Can we use precipitation isotope outputs of Isotopic General Circulation Models to improve hydrological modeling in large mountainous catchments on the Tibetan Plateau?

Yi Nan[1], Zhihua He[2], Fuqiang Tian[1], Zhongwang Wei[3], Lide Tian[4]

[1] Department of Hydraulic Engineering, State Key Laboratory of Hydroscience and Engineering, Tsinghua University, Beijing 100084, China

[2] Center for Hydrology, University of Saskatchewan, Saskatchewan, Canada

[3] Guangdong Province Key Laboratory for Climate Change and Natural Disaster Studies, School of Atmospheric Sciences, Sun Yat-sen University, Guangzhou, Guangdong, China

[4] Institute of International Rivers and Eco-security, Yunnan University, Kunming, China

***Corresponding to*:** Fuqiang Tian

Address: Room 330 New Hydraulic Building, Tsinghua University, Beijing 100084, China

Email: tianfq@mail.tsinghua.edu.cn

Abstract

Issues related to large uncertainty and parameter equifinality have posed big challenges for hydrological modeling in cold regions where runoff generation processes are particularly complicated. Tracer-aided hydrological models that integrate transportation and fractionation processes of water stable isotope are increasingly used to constrain parameter uncertainty and refine the parameterizations of specific hydrological processes in cold regions. However, commonly unavailability of site sampling of spatially distributed precipitation isotope hampers the practical applications of tracer-aided models in large scale catchments. This study, taken the precipitation isotope data (isoGSM) derived from the Isotopic General Circulation Models (iGCM) as an example, explored its utility in driving a tracer-aided hydrological model in the Yarlung Tsangpo River basin (YTR, around 2×10^5 km^2 with mean elevation of 4875 m) on the Tibetan Plateau (TP). The isoGSM product was firstly corrected based on the biases between gridded precipitation isotope estimates and limited site sampling measurements. Model simulations driven by the corrected isoGSM data were then compared with those forced by spatially interpolated precipitation isotope from site sampling measurements. Our results indicated that: (1) spatial precipitation isotope derived from the isoGSM data helped to reduce modeling uncertainty and improve parameter identifiability in a large mountainous catchment on the TP, in comparison to a calibration method using discharge and snow cover area fraction without any information of water isotope; (2) model parameters estimated by the corrected isoGSM data presented higher transferability to nested sub-basins and produced higher model performance in the validation period than that estimated by the interpolated precipitation isotope data from site sampling measurements; (3) model calibration forced by the corrected isoGSM data successfully rejected parameter sets that overestimated glacier melt contribution and gave more reliable contributions of runoff components, indicating the corrected isoGSM data served as a better choice to provide informative spatial precipitation isotope than the interpolated data from site sampling measurements at macro scale. This work suggested plausible utility of combining isoGSM data with measurements even from a sparse sampling network in improving hydrological modeling in large high mountain basins.

Key word

Tracer-aided hydrological modeling; Large basins on the Tibetan Plateau; Isotopic General Circulation Models (iGCM) product; iGCM correction with sparse measurements.

1. Introduction

Large uncertainty and strong equifinality of parameter calibration are the widely recognized issues in hydrological modelling (Gupta et al., 2008), especially in cold regions where hydrological complexity is highly enhanced by the competitions of multiple water inputs and the strong spatio-temporal variabilities of runoff generation processes (Li et al., 2019). Tracer-aided hydrological models integrating a water or environmental tracer (e.g., stable oxygen isotope, $\delta^{18}O$) module into the runoff generation architecture have been proved as highly valuable in improving parameter calibration and diagnosing model uncertainty (Son and Sivapalan, 2007; Birkel et al., 2011; Capell et al., 2012; He et al., 2019). Multiple-objective calibration of tracer-aided model towards both runoff and isotope simulation allows for rejection of parameters based on runoff observation alone, consequently makes the model satisfy multiple objectives and reduces the model uncertainty (McGuire et al., 2007). However, practical applications of tracer-aided hydrological modeling are mainly limited in only small to meso scales. The largest basin area where previous tracer-aided modelling has been implemented is around 10^3 km^2 (i.e., Delavau et al., 2017; Campell et al., 2012; Stadnyk et al., 2013). Reasons fall in either the lumped conceptual model structures due to the complicated tracer processes difficult to be coupled with distributed model (Birkel and Soulsby, 2015), or the low availability of tracer data in large basins due to difficulties in the long-term, continuous and high-frequency field sampling works (e.g., Ala-aho et al., 2017; He et al., 2019). The structure and data issues make the model not suitable for capturing the strong spatial variability of hydrological behaviors in large scale basins.

The Tibetan Plateau (TP) is the source region of many large rivers (e.g., Brahmaputra, Ganges, Indus, Mekong, among others), which sustain the ecosystems and provide a great proportion of water source for downstream livelihoods and agricultural irrigation (Zhang et al., 2013; Schaner et al., 2012). Decision making of water resource management over TP and its downstream area relies heavily on river runoff in the large basins. Meanwhile, melting water from snow and ice contributes a significant proportion to river runoff in the large basins on TP due to the cold climate and glacier coverage in head watersheds (Li et al., 2019). Runoff in this region is thus highly vulnerable to climate warming. Robust quantification of the contribution of meltwater to river runoff is critical in understanding water resources dynamics on TP (Immerzeel et al., 2013). Although great efforts have been conducted to quantify the contributions of runoff components and their future trends under climate changes on TP (e.g., Immerzeel et al., 2010; Lutz et al., 2014; Su et al., 2016; Masood et al., 2015), results reported in the wide range of studies show substantial differences (Xu et al., 2019; Tian et al., 2020). The disagreement among studies indicates big challenges on quantifying contributions of runoff

components and predicting their future trend in the large basins on TP. The difficulty of this task is mainly related to the large uncertainty of hydrological modelling and parameter calibration in the TP, because of the complex hydrological processes (He et al., 2018) and the commonly inaccurate estimation of precipitation (Xu et al., 2017; He et al. 2017). The strong inter-competitions of runoff processes induced by meltwater versus rainwater and surface water versus subsurface water were inadequately constrained in hydrological models by the commonly used hydrological observation of streamflow (Duethmann et al., 2015), and even additional data of snow/ice coverage (He et al. 2019). Reducing the modelling uncertainty originated from parameter calibration is essential for proper understanding of runoff regimes and robust prediction of future hydrological change.

Tracer-aided hydrological models that additionally involved water stable isotope data for parameter calibration have been proved as highly capable on constraining the inter-competitions of runoff processes induced by meltwater and rainwater in high mountains (He et al. 2019; Nan et al. 2021), which, however, have not been tested in large basins yet due to the unavailability of precipitation isotope data. Global gridded isotope product potentially serves as an alternative forcing of precipitation isotope data for tracer-aided hydrological models in large basins where high-frequency sampling work in a large region is not feasible. One of these options comes to outputs of the isotopic General or Regional Circulation Models (iGCM and iRCM, Noone and Sturm, 2010; Xi, 2014; Sturm et al., 2005, 2007), which has been proved to have high performance on simulating the seasonal and spatial variations of isotopic signature of precipitation on regional and global scales (Wang et al., 2017; Yao et al., 2013). However, very few works have been conducted to test the behavior of such products on forcing hydrological models. To the best of our knowledge, the only one work was conducted by Delavau et al. (2017), who examined the performance of an iRCM product REMOiso on forcing tracer-aided model in a regional catchment of around 10^3 km^2 in Canada. Their results indicated that hydrological simulations driven by the iRCM product reproduced the variations of isotopic signature ($\delta^{18}O$) of river water comparably to the simulations driven by $\delta^{18}O$ measurements from sampling sites and improved the representations of internal hydrological processes in the model. Those attempts provide sound confidences for exploring the utility of global and regional gridded isotope data products in aiding hydrological modeling in large basins on TP.

Motivated by the mentioned backgrounds, we adopted a tracer-aided hydrological model developed by Nan et al. (2021) to simulate runoff processes and the contributions of runoff components to streamflow in a large basin extending around 2×10^5 km^2 on the TP. The isotope module was driven by two kinds of precipitation isotope data including site measurements from water samples and outputs of iGCM. Scientific questions addressed in this study are two-fold: (1) what are the benefits of involving water isotope data for hydrological modeling in larger catchments? (2) how does the gridded precipitation isotope data of iGCM products perform on

forcing tracer-aided hydrological model in large basins?

2. Materials and methodology

2.1 Study area

The Yarlung Tsangpo River (YTR) located in the southern TP on the north of Himalaya Mountain (Fig. 1) is one of the longest rivers (longer than 2000 km) originating from TP. The YTR basin is located in the range of 27-32°N and 82-97°E, with an elevation range of 2900-6900 m a. s. l. The mean annual precipitation in YTR basin is around 470 mm, which is dominated by South Asian Monsoon in the Indian Ocean hydrosphere-atmosphere system, resulting in obvious wet season from June to September (Dong et al., 2016). Contributing area to the Nuxia hydrological station extends approximately 2×10^5 km^2, around 2% of which is covered by glacier. Plenty of previous works have shown the great contribution of snow and glacier melting to the runoff in YTR (e.g., Chen et al., 2017; Tian et al., 2020).

The Karuxung River (KR) catchment is located in the upper region of YTR basin, on the northern slope of the Himalayan Mountains, which is used for model evaluation in sub-basin because of its high glacierized area proportion (around 20%). The KR originates from the Lejin Jangsan Peak of the Karola Mountain at 7206 m above sea level (a.s.l.), and flows into the Yamdrok Lake at 4550m a.s.l. (Zhang et al., 2006a). The KR catchment covers an area of 286 km^2. Runoff in KR catchment is strongly influenced by the headwater glaciers which cover an area of around 58 km^2.

[Figure 1]

2.2 Hydro-meteorological data and site water sampling for isotope analysis

Digital elevation model (DEM) data in the YTR catchment with a spatial resolution of 30-m was extracted from the Geospatial Data Cloud (http://www.gscloud.cn). The 3-hour 0.1°×0.1° China Meteorological Forcing Dataset (CMFD) which combined multiple datasets (e.g., GLDAS and TRMM) with the national meteorological station data (Yang et al., 2010) provided meteorological inputs including precipitation, temperature and potential evapotranspiration. Glacier coverages were extracted from the Second Glacier Inventory Dataset of China (Liu, 2012). The Tibetan Plateau Snow Cover Extent product (TPSCE, 5km×5km, Chen et al., 2018) were used to denote the fluctuations of daily snow cover area (SCA) in the basins, which also included the glacier cover area. The 8-day Leaf Area Index (LAI) and the monthly normalized difference vegetation index (NDVI) data were downloaded from MODIS products of MOD15A2H (500m×500m, Myneni et al., 2015) and MOD13A3 (1km×1km, Didan, 2015), respectively. Soil parameters were estimated based on the soil properties extracted from the 1km × 1km Harmonized World Soil Database (HWSD, http://www.fao.org/geonetwork).

Daily streamflow during 2000-2010 for hydrological calibration were observed at the

Nuxia, Yangcun and Nugesha hydrological stations. Grab samples of precipitation and stream water were collected in 2005 at four stations along the main stream of YTR, i.e., Lazi (4889 m a.s.l.), Nugesha (4715 m a.s.l.), Yangcun (4541 m a.s.l.) and Nuxia (3691 m a.s.l.), from the upstream to the downstream (Fig. 1). Precipitation water were sampled as immediately as possible after the precipitation events, and stream water samples were collected weekly every Monday from the river. Considering the continental effect and elevation effect on precipitation isotope, the measured isotopic composition of precipitation from site sampling was interpolated by longitude and altitude (similar with Zhao et al. 2012, Liu et al. 2014) using Eq. 1 to provide spatial precipitation isotope for model input, in which the coefficients *x*, *y* and *z* were estimated by least squares fitting the average precipitation $\delta^{18}O$ and corresponding altitude/longitude at the four measuring stations. The coefficient x reflected the altitudinal lapse of precipitation isotope, thus was expected to be lower than zero. Longitude reflected the distance from the station to the mainland border, thus the coefficient y was expected to be larger than 0. The term latitude was not chosen as a regression variable, because of the similar latitude of the measurement stations and the relatively narrow north-south range of the basin (Fig. 1). Isotopic composition of glacier meltwater was assumed to be constant during the entire study period, and lower than the amount weighted average isotopic composition of precipitation.

$$\overline{\delta^{18}O_{precipitation}}(‰) = x * ALT(m) + y * LON(°E) + z \quad (1)$$

Daily temperature and precipitation in the KR catchment during 2006-2012 were collected at the Langkazi meteorological Station. Altitudinal distributions of temperature and precipitation across the catchment were estimated by the lapse rates reported in Zhang et al. (2015). Daily streamflow during 2006-2012 for hydrological calibration and evaluation were measured at the Wengguo hydrological station. Grab samples of precipitation and stream water at the Wengguo Station in 2006-2007 and 2010-2012 were collected for isotope analysis. Isotopic composition of precipitation over elevation bands was calculated from the sampling site of Wengguo Station using an altitudinal lapse of -0.34‰/100m reported in Liu et al. (2007). Isotopic composition of glacier meltwater in this catchment was assumed to be -18.9‰, constantly throughout the entire study period, adopting from the value reported in Gao et al. 2009). Details of water samples in YTR and KR catchments are summarized in Table 1.

[Table 1]

2.3 Isotopic General Circulation Model isoGSM and bias correction

Precipitation $\delta^{18}O$ of the Scripps global spectral model with water isotopes-incorporated (isoGSM) developed by Yoshimura et al. (2008) was extracted to drive the tracer-aided model. IsoGSM was developed from the Scripps Experimental Climate Prediction Center's GSM, which was based on the medium range forecast model for making operational analysis and predictions (Kanamitsu et al., 2002). Wang et al. (2017) evaluated the performance of ten iGCM

datasets in five aspects of average isotope simulation, seasonal difference, temperature effect, precipitation effect and the global meteoric water line, ranking isoGSM as 1, 2, 1, 2 and 2 respectively, indicating a relatively best performance of isoGSM among the iGCMs. The spatial and temporal resolutions of isoGSM dataset are 1.875°×1.875° and 6 hours, respectively.

The precipitation $\delta^{18}O$ estimated by isoGSM was corrected by site sampling measurements in Eqs. 2-4 before being used for hydrological model input. Biases between the amount weighted averages of isoGSM isotope and sampling measurement at the four sampling sites in YTR basin were calculated in Eq. 2 first. Spatial distribution of bias between isoGSM isotope and sampling measurement was then assumed as linearly related to altitude in Eq. 3, in which the coefficients of *a* and *b* were estimated by least squares fitting the site biases calculated in Eq. 2 and corresponding site altitudes. Daily isoGSM isotope data in hydrological model units over the study catchment were finally corrected in Eq. 4 using the unit altitudes.

$$bias_i = \overline{\delta^{18}O_{i,m}} - \overline{\delta^{18}O_{i,G}} \quad i = 1,2,3,4 \tag{2}$$

$$bias\_r = a * ALT + b \tag{3}$$

$$\begin{cases} bias\_r_k = \delta^{18}O_{k,j,G} + a * ALT_k + b \\ \delta^{18}O_{k,j,Corr} = \delta^{18}O_{k,j,G} + bias\_r \end{cases} \tag{4}$$

where, $\overline{\delta^{18}O_{i,m}}$ is the amount weighted average of measured precipitation isotope over the sampling period in sampling site *i* (*i*=1-4), and $\overline{\delta^{18}O_{i,G}}$ is the amount weighted average of isoGSM precipitation isotope over the study period in pixel that contains the sampling site *i*. *ALT* is altitude of the sampling site or hydrological model unit. Parameters *a* and *b* are the linear regression coefficients. $\delta^{18}O_{k,j,Corr}$ and $\delta^{18}O_{k,j,G}$ are the corrected and original isoGSM precipitation isotope at all the hydrological model unit *k* (*k*=1-63) on the j^{th} day, respectively. Performance of the correction method of isoGSM data was evaluated by sampling measurement of precipitation isotope at the Wengguo station in the KR sub-basin, which was not involved in the estimation of coefficients *a* and *b* in Eq. 3. Spatial precipitation isotope of the isoGSM data in the KR sub-basin for hydrological modeling was estimated using the same altitudinal lapse that was used to interpolate the sampling data in Section 2.2, because the KR catchment only encompasses one pixel of the isoGSM data.

2.4 Tracer-aided hydrological model

A distributed tracer-aided hydrological model THREW-t (Tian et al., 2006; Nan et al., 2021) was adopted in this study for streamflow and isotope simulations. This model uses the Representative Elementary Watershed (REW) method for the spatial discretization of catchment, in which the study catchment is first divided into REWs based on the catchment DEM. Each REW is further divided into two vertical distributed layers (surface and subsurface layers), including eight hydrological sub-zones according to land covers and soil properties

within the REW. Hydrological processes including canopy interception, infiltration, infiltration-excess runoff, saturation-excess runoff and groundwater outflow were simulated in each REW. REW is based on the self-similar characteristics of a watershed and its sub-watersheds (Reggiani et al., 1999), and is regarded as the fundamental component of hydrological processes and modelling, in which series of balance equations are established. The principle of REW division is based on the scale of interest, modelling purpose, and the data availability (Tian et al., 2006, 2008). In total, 63 and 41 REWs were extracted in YTR and KR, respectively, which were adopted in two previous studies (Tian et al., 2020; Nan et al., 2021). Areal averages of the gridded estimates of CMFD meteorological variables and precipitation $\delta^{18}O$ were used in each of the REWs to drive the hydrological model. For application in cold and high regions, a module representing the glacier melting and snowpack evolution was incorporated into the original model in Tian et al. (2006), which has been proved as successful in previous modelling works (e.g., He et al., 2015; Xu et al., 2019; Tian et al., 2020). The semi-distributed REW-based structure made the model concise enough to couple the tracer module easily. The tracer module was developed by Nan et al. (2021) which performed quite well on reproducing the isotopic signature of stream water in the KR catchment. The isotope mixing and fractionation processes were simulated based on the completely mixing assumption and the Rayleigh fractionation method (Hindshaw et al., 2011; Wolfe et al., 2007). Forced by the input data of precipitation isotope composition, the model can simulate the isotopic evolution all the water bodies in the watershed, including soil water, snowpack, stream water, etc. The THREW-t model considered the runoff components to stream water based on two aspects (Nan et al., 2021). First is based on the individual water sources in the total water input forcing runoff processes including rainfall, snowmelt and glacier melt. Second is based on the runoff-generation processes including surface runoff and subsurface runoff (baseflow). The THREW-t model mainly described the rainfall-runoff processes, thus only the role of shallow groundwater which can be recharged by the rainfall was considered, but the contribution from deep groundwater storage was not simulated. More details of model description and set up are given in Tian et al. (2006) and Nan et al. (2021).

The physical basis and value ranges of the calibrated parameters in the THREW-t model are described in Table 2. In both modeling catchments of YTR and KR, the parameter values were optimized using three calibration variants: (1) a dual-objective calibration using observed discharge and MODIS snow covered area fraction (SCA), (2) a triple-objective calibration using observed discharge, MODIS SCA and $\delta^{18}O$ measurements of stream water forced by linearly interpolated measurements of site sampling precipitation isotope, and (3) a triple-objective calibration using observed discharge, MODIS SCA and $\delta^{18}O$ measurements of stream water but forced by the isoGSM precipitation isotope data. Metrics used to evaluate the simulations of discharge, SCA and isotope are list in Eqs. 5-7.

$$NSE_{dis} = 1 - \frac{\sum_{i=1}^{n}(Q_{o,i} - Q_{s,i})^2}{\sum_{i=1}^{n}(Q_{o,i} - \overline{Q_o})^2} \quad (5)$$

$$RMSE_{SCA} = \sqrt{\frac{\sum_{i=1}^{n}(SCA_{o,i} - SCA_{s,i})^2}{n}} \quad (6)$$

$$MAE_{iso} = \frac{\sum_{i=1}^{n}|\delta^{18}O_{o,i} - \delta^{18}O_{s,i}|}{n} \quad (7)$$

where, n is the total number of observations. Subscripts of o and s refer to observed and simulated variables, respectively. $\overline{Q_o}$ is the average value of observed streamflow during the assessing period.

[Table 2]

An automatic procedure based on the pySOT optimization algorithm developed by Eriksson et al. (2015) was implemented for all the three calibration variants to identify the behavioral parameters. The pySOT used surrogate model to guide the search for improved solutions, with the advantage of needing few function evaluations to find a good solution. An event-driven framework POAP were used for building and combining asynchronous optimization strategies. The optimization was stopped if a maximum number of allowed function evaluations was reached, which was set as 3000 in this study. For both modeling catchments, the pySOT algorithm was repeated 150 times for each calibration variant. Although the measurement unit of NSE_{dis} is different from $RMSE_{SCA}$ and MAE_{iso}, their values are in the same order of magnitude (0-1) when the model performances were acceptable (Ala-aho et al., 2017; Nan et al., 2021). Consequently, they were combined with equal weights for simplification to represent the simultaneous performance on multiple objectives. For the dual- and triple-objective calibration variants, NSE_{dis} - $RMSE_{SCA}$, NSE_{dis} - $RMSE_{SCA}$ - MAE_{iso} were chosen as combined optimization objectives, respectively. Among the 150 final parameter sets produced by the pySOT runs, the behavioral parameter sets were selected by NSE_{dis} thresholds, i.e., only the parameter sets producing NSE_{dis} higher than an assumed threshold were regarded as behavioral parameter sets. Considering the model behaviors in the two catchments, the NSE_{dis} threshold was chosen as 0.85 for the YTR basin, and was chosen as 0.75 and 0.70 for dual- and triple-objective calibration variants in KR catchment, respectively. Focusing on the utility of isoGSM on forcing tracer-aided model, the influence of calibration objective function and weight of each objective were not assessed in this study.

Considering the data availability, the calibration and validation periods for KR catchment were set as 2006-2010 and 2011-2012, respectively. For YTR basin, discharge measured at the outlet station Nuxia, the MODIS SCA fraction over the basin area upper the Nuxia station, and the stream water $\delta^{18}O$ measured at the Nuxia station were used for calibration. Calibration and validation periods of 2001-2005 and 2006-2010 were selected to test the model performance for simulations of discharge and SCA at the Nuxia station. In addition, discharge measured at the internal hydrological stations of Yangcun and Nugesha during 2001-2010 were used to

validate the spatial consistency of the calibrated model parameters. Model performance on simulating stream water isotope at the Nuxia station in a validation period was not assessed as stream water isotope measurements were available only during 2005. However, stream water $\delta^{18}O$ measured during 2005 at the internal hydrological stations of Yangcun, Nugesha and Lazi were adopted to validate the model performance on simulating spatial stream water $\delta^{18}O$ within YTR basin.

3. Results

3.1 Comparison between isoGSM and measured precipitation $\delta^{18}O$

Figs. 2a and 3a show the comparison between isoGSM and measured precipitation $\delta^{18}O$ at four sampling sites in the YTR basin. The isoGSM data presented similar fluctuations of seasonal precipitation $\delta^{18}O$ to the sampling measurements (Fig. 3a). In particular, both isoGSM and sampling measurement showed high precipitation $\delta^{18}O$ in May, and reached relatively low values in the wet season during August and September. However, the original isoGSM data tended to overestimate the measured precipitation $\delta^{18}O$ in the sampling periods (Fig. 2a). From downstream to upstream, the amount weighted average precipitation $\delta^{18}O$ of samples collected at the four stations (Nuxia, Yangcun, Nugesha and Lazi) were -9.58‰, -14.01‰, -14.80‰ and -17.86‰, respectively, while the corresponding weighted average values of isoGSM pixels containing the sampling stations during the same period were -7.53‰, -8.38‰, -9.22‰ and -9.61%, respectively. Bias between isoGSM data and sampling measurement tended to be larger at upstream stations with higher elevations, partly due to the coarse spatial resolution of GCM which cannot reproduce the effect of regional topography well. In contrast, the corrected isoGSM data (black lines in Fig. 3a) captured the relatively low values in the late wet season better than the original data (grey lines in Fig. 3a), and the scatter points fall closer to the 1:1 line (Fig. 2b). The MAE of isoGSM precipitation $\delta^{18}O$ in the YTR reduced from 6.65‰ to 4.91‰ after correction. Similarly, the original isoGSM data presented comparable seasonal fluctuations of precipitation isotope to the sampling measurement at the Wengguo station in the KR catchment (Fig. 3b), but the amount weighted average of precipitation $\delta^{18}O$ in the original isoGSM data (-10.95‰) is much higher than that in the sampling measurement (-15.97‰, Fig. 2c and 3b). After bias correction, the overestimation was much reduced (Fig. 2d), indicated by a reduced MAE value from 6.24‰ to 4.47‰. Underestimation of precipitation $\delta^{18}O$ by the original isoGSM data in springs of 2011 and 2012, however, was not improved by the bias correction.

[Figure 2]

[Figure 3]

Based on the multiple linear regression, the coefficients x, y and z in Eq. 1 were estimated

as -0.003, 0.574 and -52.6, respectively, with a R^2 value of 0.98, to interpolate the measured isotope data to estimate spatial precipitation isotope over the YTR basin. The negative *x* and positive *y* values were consistent with their physical meanings. Parameters *a* and *b* in Eq. 3 were estimated as -0.0046 and 14.96 based on the biases between isoGSM data and sampling measurements on the four sampling sites in YTR. Fig. 4 and Fig.5 show the comparison of the amount weighted averages of precipitation $\delta^{18}O$ on 63 REWs derived from the corrected isoGSM data and interpolated sampling measurement. It is shown that the distributions of precipitation isotope with altitude were rather similar in the two datasets (Fig. 4b). However, distributions across the longitudes show visible differences. The largest differences between the two datasets were located in the west upstream region (longitude < 86°) and the source region of tributary Lhasa River (93° > longitude > 86°, latitude > 30°) (Fig. 4a and 5). In comparison to the corrected isoGSM data, the interpolated sampling measurement estimated much lower isotope signature in the upstream region, while presenting higher isotope signature in the upper Lhasa River. As site sampling data of precipitation was insufficient to test which of the two datasets captured the west-east distribution of precipitation isotope better, model performance on simulating isotope signatures of stream water measured at hydrological stations from west to east forced by the two datasets provide a perspective to assess the precipitation isotope estimations.

[Figure 4]

[Figure 5]

3.2 Model performance for the simulations of discharge and stream water isotope

Fig. 6-7 and Table 3 show the model performance of different calibration variants in the YTR basin produced by the behavioral parameter sets. The three calibration variants produced similar simulations of discharge and SCA (Fig. 6), in spite of the slightly higher NSE_{dis} and lower $RMSE_{SCA}$ estimated by the dual-objective calibration (Table 3). For the simulation of stream water $\delta^{18}O$, the dual-objective calibration produced the worst MAE_{iso} values in three out of the four testing stations with the largest uncertainty ranges (Fig. 7a), which can be expected as isotope data was not involved in this calibration. The two triple-objective calibration variants produced good simulation for the stream water isotope at the Nuxia station in the calibration year of 2005 (Fig. 7b and 7c). However, the triple-objective calibration variant forced by isoGSM data estimated worse performance (i.e., higher MAE_{iso} values) for stream water $\delta^{18}O$ at the stations of Yangcun and Nugesha than the calibration forced by interpolated sampling measurement showing significant underestimations for peak isotope values in June at Yangcun station, and higher overestimations for isotope values after August at Nugesha. This was due to the poor performance of isoGSM on capturing the isotope signature of individual precipitation events during a specific period (see Fig. 3a), although being corrected already. For example,

the amount weighted average of measured precipitation $\delta^{18}O$ in June at the Yangcun station was -5.87‰, while the average of corrected isoGSM data showed a value of -10.09‰, leading to an underestimated peak value. Similarly, the amount weighted average of measured precipitation $\delta^{18}O$ at Nugesha during August was -16.34‰, while the corrected isoGSM data estimated an average of -11.47‰, leading to an overestimated stream $\delta^{18}O$ in the late wet season. In spite of that, the performance of simulated stream water $\delta^{18}O$ at Nuxia, Yangcun and Nugesha stations forced by corrected isoGSM data can still be considered as acceptable, given the MAE_{iso} values were generally around 1 (Fig. 7c). For the most upstream station Lazi, however, the triple-objective variant forced by measured precipitation $\delta^{18}O$ produced significantly underestimated $\delta^{18}O$ of stream water, likely due to the underestimated precipitation $\delta^{18}O$ in the upstream high altitudes produced by the interpolated measurement data (Fig. 4a and 5). The good performance of simulated stream water $\delta^{18}O$ at the Lazi station driven by the corrected isoGSM data demonstrated that the corrected isoGSM estimated a better precipitation isoscape in high altitudes of the study catchment than the linearly interpolated measurement data, partly benefiting from the information of spatial precipitation isotope implied in the gridded values. It is worth noting that the model simulations forced by corrected isoGSM estimated narrower uncertainty bands for stream water $\delta^{18}O$ at Nuxia, Yangcun and Nugesha, and smaller value ranges of the MAE_{iso} metric at all the four stations, in comparison to the simulations driven by the interpolated precipitation $\delta^{18}O$. Compared to the simulations yielded by the dual-objective calibration, the triple-objective calibration variants simulated smaller uncertainty ranges for stream water $\delta^{18}O$ and slightly narrowed value ranges of objective metrics for the simulations of discharge and SCA with the lower behavioral ratios of calibrated parameter sets in Table 3, indicating good potential of isotope data on reducing modeling uncertainty and improving parameter identifiability.

[Figure 6]

[Figure 7]

[Table 3]

The simulated hydrographs at two internal hydrological stations of Yangcun and Nugesha were compared in Fig. 8 to assess the spatial consistency of model parameters calibrated by the different variants. The isoGSM-forced triple-objective calibration produced the highest performance for discharge simulation at the two internal stations (Fig. 8e and 8f) indicated by the highest averages (0.82 and 0.74 for Yangcun and Nugesha) and minimal values (0.72 and 0.53 for Yangcun and Nugesha) of NSE, as well as the smallest values ranges of NSE. The dual-objective calibration produced lower performance for discharge simulation than the isoGSM-forced triple-objective calibration (with average NSE as 0.8 and 0.67 at Yangcun and Nugesha) with a much larger uncertainty of the baseflow simulation (Fig. 8a and Fig. 8b). The interpolation-forced triple-objective calibration produced higher mean NSE (0.81 and 0.74 for

Yangcun and Nugesha) but smaller minimal NSE (0.62 and 0.31 for Yangcun and Nugesha) than the dual-objective calibration with the largest values ranges of NSE at the two stations. Moreover, the isoGSM-forced triple-objective calibration performed best on capturing the peak flows in summer at both stations.

[Figure 8]

The model performances produced by the behavioral parameter sets of different calibration variants in the KR catchment were shown in Figs. 9-10 and Table 4. All the three calibration variants presented similar performances on simulating streamflow, while the two triple-objective calibrations resulted in narrower uncertainty ranges, especially for the baseflow (Fig. 9c and e). The declining SCA in spring-summer was captured well in all the calibration variants (Figs. 9b, d and f). Triple-objective calibrations driven by the two isotope datasets performed comparably well on simulating the isotopic composition of stream water in the calibration period (Fig. 10b and 10c) indicated by the low average values of MAE_{iso} (0.68 and 0.69) and the well captured seasonal fluctuations of stream water $\delta^{18}O$. The peak isotopic values in around June of 2007 were not captured well by the isoGSM-driven model (Fig. 10c), resulting in a relatively larger minimal MAE_{iso} (0.57) than the interpolated measurement-driven result (0.48). This was due to the underestimations of isoGSM on estimating the isotope signatures of individual extreme precipitation events in June (see Fig. 3b). Specifically, there was a precipitation event larger than 20mm/day in June of 2007, of which the corrected isoGSM produced significantly lower $\delta^{18}O$ (-21.55‰) than the sampling measurement (-9.83‰) at the Wengguo station. Despite that, the isoGSM-forced triple-objective calibration estimated much better performance than the interpolated measurement-driven calibration for stream water $\delta^{18}O$ in the validation period (Figs. 10b and c). Similar to YTR, the triple-objective calibrations got much smaller behavioral parameter sets (19 and 18 for measurement- and isoGSM-forced calibration variants) than the dual-objective calibration (117) through 150 runs of the automatic calibration program, indicating strongly increased identifiability of model parameters and reduced uncertainty by the using of isotope data.

[Figure 9]

[Figure 10]

[Table 4]

3.3 Contributions of runoff components

Fig. 11 and Tables 5-6 compare the proportions of water sources in the annual water input for runoff generation simulated by the behavioral parameter sets identified by the three calibration variants. In the KR sub-basin (Fig. 11b and Table 6), rainfall provided the largest volume of water source for runoff generation simulated by the three calibration variants (44.2%-47.4%), followed by glacier meltwater (29.2%-33.8%). Snowmelt contributed the

lowest proportion of 22.0%-23.4% in the total water input. The two triple-objective calibrations estimated very similar contributions of runoff component, and consistently estimated lower proportions of glacier melt than the dual-objective calibration, which can be attributed to the role of isotope data in regulating the contribution of strong-evaporated surface runoff component fed by glacier melt to streamflow (Nan et al., 2021) by rejecting parameter sets that estimated small proportions of rainfall but large proportions of glacier melt (as shown by the error bar in Fig. 11b). Meanwhile, uncertainties of the estimated contributions were significantly reduced (from 9.4% to 6.2% and 4.7%, Table 6) by integrating isotope data into the model. Regarding the contributions of water sources to seasonal water input, snowmelt and rainfall were the dominant water sources in spring and summer. Three water sources had similar contributions during autumn. Glacier melt produced a relatively steady contribution of around 30%-35% throughout the year. Similar to the annual contributions, seasonal contributions of snowmelt and rainfall estimated by the two triple-objective calibrations were larger than those estimated by the dual-objective calibration, while the opposite holds true for the seasonal contributions of glacier melt. The largest differences of the contributions estimated by the different calibration variants go to the winter season (Table 6), which however had negligible effect on the annual runoff regime because of the extremely low contribution of water input in this season (<1%). Uncertainties of the runoff component contributions were reduced by involving isotope calibration most significantly during summer, because the isotope data brought more constraint on the rainfall-runoff processes, which played dominant role in summer. The uncertainties of annual contributions were close to those of summer contributions because of the large proportion of water input to annual runoff in summer (>60%). In contrast, uncertainties of winter contributions estimated by the triple-objective calibration variants tended to be larger than that estimated by the dual-objective calibration, due to the smaller amount of total water input in winter as a result of lower contribution of meltwater estimated by triple-objective variants.

In the YTR catchment, rainfall showed larger dominance on annual runoff than glacier and snow meltwater with the mean contributions of 61.4%-69.6% (Fig. 11a and Table 5). The dual-objective calibration and triple-objective calibration forced by measured isotope data estimated similar annual contributions of rainfall (~62%), snowmelt (~11%) and glacier melt (~27%). Nonetheless, the isoGSM-forced triple-objective calibration estimated significantly higher mean proportion of rainfall (70%) but lower mean proportion of glacier melt (18%) by rejecting the parameter sets that estimated rainfall contributions less than 60% and glacier melt contributions more than 30%, which however were identified to be acceptable in the other two calibration variants (as shown by the error bar in Fig. 11a). Difference of the glacier melt contributions estimated by the two triple-objective calibration variants mainly resulted from the difference of precipitation $\delta^{18}O$ inputs from the two datasets. The interpolated measurement

data tended to produce higher precipitation $\delta^{18}O$ in the middle and downstream regions of YTR basin but lower values in the upstream region, compared to the corrected isoGSM data (Fig. 4b). Meanwhile, the precipitation input in the downstream region was higher than that occurred in the upstream (Xu et al., 2017), thus resulting in higher average precipitation $\delta^{18}O$ over the entire YTR of the interpolated measurement data. Consequently, larger contribution of glacier melt with low isotope composition was estimated in the interpolated interpolation-forced triple-objective calibration to counteract the effect of precipitation input with high isotopic composition for matching the measured stream water $\delta^{18}O$. By involving isotope simulation, both triple-objective variants significantly reduced the uncertainties of the estimated contributions (from 11.9% to 8.6% and 8.9%, Table 5). Similar to the estimated annual contributions, the isoGSM-forced triple-objective calibration estimated higher mean proportion of rainfall, lower mean proportion of glacier melt and comparable mean proportion of snowmelt in the four seasons, compared to the dual-objective calibration and triple-objective calibration forced by measured isotope data. In general, rainfall was the dominant water input source in summer and autumn, and snowmelt dominated the runoff in winter. The contributions of rainfall and snowmelt to total water input were close in spring. Similar to KR catchment, uncertainty of runoff component contribution was reduced by the isotope-involved calibrations more significantly in seasons when rainfall played dominant roles.

[Figure 11]

[Table 5]

[Table 6]

4. Discussion

4.1 Uncertainties and limitations of the tracer-aided hydrological model

Integrating the simulations of water isotope signatures into the hydrological model structure could help to make use of hydrological information additionally implied in the water isotope data without introducing new model parameters for the runoff processes. However, uncertainty of the simulation of water isotope in the tracer-aided hydrological model can be caused by the following sources. First, the isotopic compositions of meltwater sources were determined based on simplified assumptions, which however were hard to verify in a large basin due to the limited field sampling work. The isotopic compositions of glacier melt were assumed as constant throughout the modeling period due to the unavailability of glacier melting water samples. Large number of studies reported that the isotope composition of glacier melt had very small variability, and the value were much lower than that of precipitation (e.g., Boral & Sen, 2020; Cable et al., 2011; He et al., 2019; Rai et al., 2019; Wang et al., 2016). Considering that the changes of glacier elevation during the 10-year modeling period were small, indicating

that ice melt on the glacier surface in each of the summer seasons occurred very likely from the same elevation bands with similar isotopic compositions, the assumption on glacier melt isotope adopted in this study was reasonable. However, the assumed isotope composition of glacier melt will no doubt influence the modelling result, especially the estimated contribution of water sources. Specifically, a lower assumed value of glacier melt isotope composition led to a lower contribution of isotopic depleted glacier melt runoff component. As for the snow meltwater, the isotopic evolution was simulated according to the mass balance of snowpack similarly with other water storages. The isotope fractionation effect caused by the melt processes was inadequately characterized in our model, which could lead to uncertainty in the simulation of snowmelt isotope (Pu et al., 2020).

Second, the uncertainty of the precipitation isotope input data served as another uncertainty source of the isotope simulation in the model. Although the isotope data itself had no influences on the hydrological processes, the calibration procedure to fit the simulated stream isotope signature with observation indeed affected the model simulations of runoff processes (Delavau et al., 2017). For the sampling measurement-based forcing data, the uncertainty came from the interpolation procedure. We used a linear interpolation method based on longitude and altitude to estimate the precipitation isoscape. This could be reasonable in our study catchment because these two factors characterize the major spatial pattern and altitude effect of precipitation isotope in similar large-scale regions on TP (Liu et al., 2014). However, low availability of site measurement data derived from the sparse water sampling network leaded to large uncertainty of the interpolated result. All the four sampling stations were located at around the same latitude, and cannot reflect latitude effect on precipitation isotope (Dansgaard, 1964). Measurements from more water sampling sites are required in the future for the improvement of the interpolation method. For the isoGSM data, uncertainty came from its coarse spatial resolution. Although the isoGSM data bears the potential to capture spatial patterns of precipitation isotope in large basins, the effect of regional topography on isotope was not reflected well in the current product due to its rather coarse pixel size (~200km×200km). Consequently, developing downscale methods that are applicable to mountainous catchments to extract regional isotope estimates from iGCM products (such as iRCM in Sturm et al., 2007) might be helpful for the tracer-aided hydrological modelling on the TP. Moreover, the bias-correction procedure based on measurements from a sparse water sampling network inevitably brought uncertainty to the corrected isoGSM data. The current sampling sites of precipitation are located along the river channel with elevations lower than the contributing mountains, thus failing to involve isoGSM estimates at high mountainous terrains into the correction procedure. The terms used in Eq. 3 (only elevation) to correct isoGSM were different from that in Eq. 1 (elevation and longitude) to interpolate the measurement data. The error of isoGSM tended to be larger in higher elevation regions, because of the complex regional topography which cannot be captured well by the

coarse spatial resolution of isoGSM, but there was no mechanism making the error of isoGSM change with longitude. Consequently, the term longitude was deprecated in Eq. 3 rather than the interpolation equation. However, the choice of regression terms in interpolation and bias correction undoubtably had significant influence on the modelling result, which could be another important source of uncertainty.

The modelling uncertainty is highly related to the model structure and parameters, and our results indicated that the additional information from isotope data reduced uncertainty of parameters. However, global climate changes are changing streamflow regimes on the TP (e.g., Xu et al., 2019; Lin et al., 2020; Yong et al., 2021), which may request a changing model structure as well. In this study, the model structure was not modified, thus the changing conditions were far less than adequately represented in the current model, due to lack of adequate understanding of the influence of changing condition on runoff generation mechanism. However, some of the changing underlying conditions can also be reflected by the parameters. For example, frozen ground degradation can lead to a larger water storage capacity and higher hydraulic conductivity, which can be reflected by the parameters WM, KKA and KKD in our model. Meanwhile, the tracer-aided hydrological modelling method can also help diagnose the model structure (e.g., Birkel et al., 2011), but such work has been only conducted in small catchments due to the limited precipitation isotope input data in large scale. This study mainly explored the utility of iGCM data on forcing tracer-aided model in large basins, thus provided the potential to conduct the works improving model structure in large basin scale. For the simulation in YTR basin in this study, the model was applied at a relatively short time scale (less than one decade), during which the change condition was not an important issue. To expand the result to a longer time scale and to predict the future streamflow trend, more work is needed to consider the variation of model structures and parameters.

4.2 The value of spatial precipitation isotope data derived from iGCM for aiding hydrological modeling in large basins

Comparisons with the dual-objective calibration without isotope data indicated high value of spatial precipitation isotope data for reducing modeling uncertainty. To better understand the role of isotope data, we analyzed the relationship between the behaviors of discharge and isotope simulations obtained by the calibration without isotope (dual-objective calibration). There was a trade-off between the two objectives (Fig. 12a). The highest NSE_{dis} can reach around 0.93, but the MAE_{iso} was not good at the same time. When MAE_{iso} reach relative best values, the NSE_{dis} was around 0.9, which exhibited a high-level performance as well. The relationship between model performance and estimated glacier melt contribution was further explored, and it was found that when the highest NSE_{dis} was obtained, the contribution of glacier melt was estimated as around 0.35~0.4, which was however estimated as around 0.2

when best MAE_{iso} was obtained (Fig. 12b and c). The isotope composition of glacier melt was assumed to be lower than the precipitation, thus an overestimated contribution of glacier melt can lead to lower simulated river isotope than measurement. Consequently, calibration focusing only on discharge may result in overestimated glacier melt, which can be rejected by the behavior of isotope simulation. It is notable that the performance of isotope simulation is more sensitive than discharge simulation to the runoff component and internal processes. When the contribution of glacier melt is in a large range of 10-40%, the NSE_{dis} can all be calibrated to a high value (>0.9) by adjusting other parameters, whereas the MAE_{iso} gets worse significantly when the proper contribution of water source is deviated.

[Figure 12]

Model simulations forced by the two precipitation isotope datasets produced similar total streamflow simulation in the YTR basin, but resulted in certain difference in the simulated stream water isotopic composition and water source apportionments, which was consistent with the findings in Delavau et al. (2017). The choice of precipitation isotope input data was demonstrated to have large influence on the model performance. In this study, model simulations forced by the corrected isoGSM data performed better than that driven by the interpolated data of sampling measurement with respect to discharge and stream water isotope simulations at internal hydrological stations. The fact that model can simultaneously satisfy multiple calibration objectives gave confidence in the model realization and robustness (McDonnell and Beven, 2014), consequently resulting in the consistent model behavioral performances in both outlet and internal stations.

Beyond the model performance on discharge and isotope simulation, three aspects of evidences indicated the results of model forced by isoGSM data to be more likely reasonable. Firstly, the runoff component contributions estimated by the isoGSM-forced triple-objective calibration were likely more reliable than those estimated by the dual-objective and the interpolation-forced triple-objective calibrations. Contribution of glacier melt to annual water input in the YTR basin was estimated as around 27% in the dual-objective and the interpolation-forced triple-objective calibrations, which was more unlike to be true considering the small glacier covered area ratio (2%). Glacier melt contribution estimated by the isoGSM-forced triple-objective calibration was lower than 20%, within the ranges reported by some previous studies (Immerzeel et al., 2010; Bookhagen and Burbank, 2010; Zhang et al., 2013). Secondly, the average calibrated melting threshold temperature (T_0) and glacier degree-day factor (DDF_G) of YTR basin obtained by the isoGSM-forced triple-objective calibration were 0.75℃ and 7.43mm/d/℃. This was consistent with the reported results estimated in a manner by glacier mass balance measurements, that the YTR basin was in the region with DDF_G ranging from 6-9 mm/d/℃ estimated by the T_0 of 0℃ (Zhang et al., 2006). On the contrary, although the calibrated DDF_G obtained by dual-objective and interpolation-forced triple-objective

calibration were still within the range of 6-9 (7.98 and 8.37 mm/ d/°C, respectively), the T_0 values were calibrated as -1.41 and -1.49°C, respectively, much lower than the value adopted in Zhang et al. (2006), resulting in overestimated glacier melt runoff. Thirdly, the THREW-t model also quantified the runoff component in terms of runoff generation pathway, and divided the runoff into surface runoff and baseflow. The contribution of baseflow was estimated as 29.26 km^3/yr by the isoGSM-forced triple-objective calibration, which was very close to the result (30km^3/yr) estimated by the groundwater model MODFLOW-NWT independently from hydrological modeling approach reported in Yao et al. (2021), whereas the baseflow estimated by dual-objective and interpolation-forced triple-objective were much lower (24.04 and 22.47 km^3/yr, respectively). A more reliable baseflow estimation likely helped improve the reasonability of modelling result, and reduce equifinality by constraining the parameters related to groundwater.

Above results indicated that the corrected isoGSM product served as a better choice to force the tracer-aided hydrological model than the interpolated data of sampling measurement. It is commonly difficult to estimate the precipitation isoscapes in large mountainous catchments according to limited available site sampling data. Relatively, the iGCM data has the advantage of presenting more spatial information of precipitation isotope via physically simulating the processes of vapor transfer, condensation and supersaturation in the atmosphere and their effects on precipitation isotope (Xi, 2014). Our results indicated that even precipitation isotope measurements at only four sampling sites provided sounds good ground data basis to correct the isoGSM isotope product in the study basin with a size of 2×10^5 km^2. The condition was different in the KR sub-catchment, where the triple-objective variants forced by two isotope datasets performed similarly with respect to discharge and isotope simulation and runoff component contribution estimation. This is due to the much smaller catchment area than the pixel size, thus the advantage of the spatial information provided by isoGSM was not taken adequately. To develop a general strategy for establishing tracer-aided in large basin, especially in the regions where limited measured precipitation isotope data is available, as less information from measurement data as possible was used to correct the isoGSM data. Consequently, only the average value of measured isotope data was used to correct the isoGSM (Eq. 2), and the seasonal characteristic of the bias was not considered (such as in Delavau et al., 2017). Our results indicated that even being corrected by only four average values, isoGSM can perform well on capturing seasonal fluctuation of precipitation isotope and forcing tracer-aided model in YTR basin, thus bears the potential to serve as input isotope data in data sparse regions. The influence of iGCM/iRCM product and bias correction method was not discussed in detail in this study, which is however an important issue and need further exploration.

5. Conclusions

The utility of precipitation isotope input derived from the Isotopic General Circulation Models (iGCM) product isoGSM in forcing the distributed tracer-aided hydrological model THREW-t in a large basin of $2\times10^5 km^2$ on the Tibetan Plateau (TP) was investigated in this study. Model performance driven by the isoGSM data was evaluated by comparing with simulations driven by precipitation isotope measurements from a sparse sampling network. Our main findings are:

(1) Spatial precipitation isotope data derived from the Isotopic General Circulation Models helped to reduce modeling uncertainty and improve parameter identifiability, in comparison to a calibration method using discharge and snow cover area fraction without any information of water isotope. The developed tracer-aided hydrological model forced by the isoGSM data showed high values for robustly representing runoff processes in large mountainous catchments.

(2) Model parameters estimated by the isoGSM data corrected using site sampling measurements of precipitation isotope presented higher transferability to nested sub-basins and produced higher model performance in the validation period than that estimated by the interpolated isotope data from site sampling measurement. The smaller uncertainty ranges of model simulations in nested sub-basins forced by the corrected isoGSM data further indicated that the corrected isoGSM data served as a better choice to provide informative spatial precipitation isotope in large basins than the interpolated data from site sampling measurements.

(3) Using the corrected isoGSM data improved the quantification of contributions of runoff components to streamflow on both annual and seasonal scales. Model calibration procedure forced by the corrected isoGSM data successfully rejected parameter sets that estimated overestimation of glacier melt contribution, indicating that precipitation isotope measurements at only four sampling sites along the river channel provided a good ground data basis to correct the isoGSM product in the study catchment.

Code/Data availability

The isotope data and the code of THREW-t model used in this study are available by contacting the authors.

Author contribution

YN, ZH and FT conceived the idea; ZW provided the isoGSM data; LT provided the measurement isotope data; YN, ZH and FT conducted analysis; ZW and LT provided comments on the analysis; all the authors contributed to writing and revisions.

Competing interests

The authors declare that they have no conflict of interest.

Acknowledgements

This study was supported by the National Key R&D Program of China（2018YFC1508103) and the National Science Foundation of China (92047301). The authors thank all the organizations and scientists for the contribution of data used in this work. All the data used in this study will be available on request from the corresponding author (tianfq@tsinghua.edu.cn).

Financial support

This study was supported by the National Key R&D Program of China（2018YFC1508103) and the National Science Foundation of China (92047301).

References

Ala-aho, P., Tetzlaff, D., McNamara, J. P., Laudon, H., & Soulsby, C. (2017). Using isotopes to constrain water flux and age estimates in snow-influenced catchments using the STARR (Spatially distributed Tracer-Aided Rainfall–Runoff) model. Hydrology and Earth System Sciences, 21(10), 5089-5110. doi:10.5194/hess-21-5089-2017

Birkel, C., & Soulsby, C. (2015). Advancing tracer-aided rainfall-runoff modelling: a review of progress, problems and unrealised potential. Hydrological Processes, 29(25), 5227-5240. doi:10.1002/hyp.10594

Birkel, C., Tetzlaff, D., Dunn, S. M., & Soulsby, C. (2011). Using time domain and geographic source tracers to conceptualize streamflow generation processes in lumped rainfall-runoff models. Water Resources Research, 47(2). doi:10.1029/2010wr009547

Bookhagen, B., & Burbank, D. W. (2010). Toward a complete Himalayan hydrological budget: Spatiotemporal distribution of snowmelt and rainfall and their impact on river discharge. Journal of Geophysical Research, 115(F3). doi:10.1029/2009jf001426

Boral, S., & Sen, I. S. (2020). Tracing 'Third Pole'ice meltwater contribution to the Himalayan rivers using oxygen and hydrogen isotopes. Geochem. Perspect. Lett, 13, 48-53.

Cable, J., Ogle, K., & Williams, D. (2011). Contribution of glacier meltwater to streamflow in the Wind River Range, Wyoming, inferred via a Bayesian mixing model applied to isotopic measurements. Hydrological Processes, 25(14), 2228-2236.

Capell, R., Tetzlaff, D., & Soulsby, C. (2012). Can time domain and source area tracers reduce uncertainty in rainfall-runoff models in larger heterogeneous catchments? Water Resources Research, 48(9). doi:10.1029/2011wr011543

Chen, X., Long, D., Liang, S., He, L., Zeng, C., Hao, X., & Hong, Y. (2018). Developing a composite daily snow cover extent record over the Tibetan Plateau from 1981 to 2016 using multisource data. Remote Sensing of Environment, 215, 284-299. doi:10.1016/j.rse.2018.06.021

Dansgaard, W.: Stable isotopes in precipitation, Tellus, 16, 436–468, 1964.

Delavau, C. J., Stadnyk, T., & Holmes, T. (2017). Examining the impacts of precipitation isotope input (δ18O) on distributed, tracer-aided hydrological modelling. Hydrology and Earth System Sciences, 21(5), 2595-2614. doi:10.5194/hess-21-2595-2017

730 Didan, K. (2015). MOD13A3 MODIS/Terra vegetation Indices Monthly L3 Global 1km SIN
731 Grid V006 [Data set]. NASA EOSDIS Land Processes DAAC. Accessed 2020-01-01 from
732 https://doi.org/10.5067/MODIS/MOD13A3.006

733 Dong, W., Lin, Y., Wright, J. S., Ming, Y., Xie, Y., Wang, B., . . . Xu, F. (2016). Summer rainfall
734 over the southwestern Tibetan Plateau controlled by deep convection over the Indian
735 subcontinent. Nature Communications, 7. doi:10.1038/ncomms10925

736 Duethmann, D., Bolch, T., Farinotti, D., Kriegel, D., Vorogushyn, S., Merz, B., . . . Güntner, A.
737 (2015). Attribution of streamflow trends in snow and glacier melt-dominated catchments
738 of the Tarim River, Central Asia. Water Resources Research, 51(6), 4727-4750.
739 doi:10.1002/2014wr016716

740 Eriksson, D., Bindel, D., & Shoemaker, C. (2015). Surrogate optimization toolbox (pysot).

741 Gao, J., Tian, L. D., & Liu, Y. Q. (2009). Oxygen isotope variation in the water cycle of the
742 Yamdrok-tso Lake Basin in southern betan Plateau. Chinese Science Bulletin, 54(15),
743 2153-2159.

744 Gupta, H. V., Wagener, T., & Liu, Y. (2008). Reconciling theory with observations: elements of
745 a diagnostic approach to model evaluation. Hydrological Processes, 22(18), 3802-3813.
746 doi:10.1002/hyp.6989

747 He, Z., Unger-Shayesteh, K., Vorogushyn, S., Weise, S. M., Kalashnikova, O., Gafurov, A., . . .
748 Merz, B. (2019). Constraining hydrological model parameters using water isotopic
749 compositions in a glacierized basin, Central Asia. Journal of Hydrology, 571, 332-348.
750 doi:10.1016/j.jhydrol.2019.01.048

751 He, Z., Vorogushyn, S., Unger‐Shayesteh, K., Gafurov, A., Kalashnikova, O., Omorova, E., &
752 Merz, B. (2018). The Value of Hydrograph Partitioning Curves for Calibrating
753 Hydrological Models in Glacierized Basins. Water Resources Research, 54(3), 2336-2361.
754 doi:10.1002/2017wr021966

755 He, Z. H., Tian, F. Q., Gupta, H. V., Hu, H. C., & Hu, H. P. (2015). Diagnostic calibration of a
756 hydrological model in a mountain area by hydrograph partitioning. Hydrology and Earth
757 System Sciences, 19(4), 1807-1826. doi:10.5194/hess-19-1807-2015

758 He, Z., Yang, L., Tian, F., Ni, G., Hou, A., & Lu, H. (2017). Intercomparisons of Rainfall
759 Estimates from TRMM and GPM Multisatellite Products over the Upper Mekong River
760 Basin. Journal of Hydrometeorology, 18(2), 413-430. doi:10.1175/jhm-d-16-0198.1

761 Hindshaw, R. S., Tipper, E. T., Reynolds, B. C., Lemarchand, E., Wiederhold, J. G., Magnusson,
762 J., . . . Bourdon, B. (2011). Hydrological control of stream water chemistry in a glacial
763 catchment (Damma Glacier, Switzerland). Chemical Geology, 285(1-4), 215-230.
764 doi:10.1016/j.chemgeo.2011.04.012

765 Immerzeel, W. W., Pellicciotti, F., & Bierkens, M. F. P. (2013). Rising river flows throughout
766 the twenty-first century in two Himalayan glacierized watersheds. Nature Geoscience, 6(9),
767 742-745. doi:10.1038/ngeo1896

768 Immerzeel, W. W., van Beek, L. P. H., & Bierkens, M. F. P. (2010). Climate Change Will Affect
769 the Asian Water Towers. Science, 328(5984), 1382-1385. doi:10.1126/science.1183188

770 Kanamitsu, M., Kumar, A., Juang, H. M. H., Schemm, J. K., Wang, W. Q., Yang, F. L., . . . Ji,
771 M. (2002). NCEP dynamical seasonal forecast system 2000. Bulletin of the American
772 Meteorological Society, 83(7), 1019-+. doi:10.1175/1520-
773 0477(2002)083<1019:Ndsfs>2.3.Co;2

774 Li Z., Qi, F., Zongjie, L., Ruifeng, Y., Juan, G., & Yuemin, L. (2019). Climate background, fact
775 and hydrological effect of multiphase water transformation in cold regions of the Western
776 China: A review. Earth-Science Reviews, 190, 33-57. doi:10.1016/j.earscirev.2018.12.004

777 Lin, L., Gao, M., Liu, J., Wang, J., Wang, S., Chen, X., & Liu, H. (2020). Understanding the
778 effects of climate warming on streamflow and active groundwater storage in an alpine
779 catchment: the upper Lhasa River. Hydrology and Earth System Sciences, 24(3), 1145-
780 1157.

781 Liu, J., Song, X., Yuan, G., Sun, X., & Yang, L. (2014). Stable isotopic compositions of
782 precipitation in China. Tellus Series B-Chemical and Physical Meteorology, 66.
783 doi:10.3402/tellusb.v66.22567

784 Liu S. (2012). The second glacier inventory dataset of China (version 1.0) (2006-2011) [Data
785 set]. National Tibetan Plateau Data Center. Accessed 2020-01-01 from
786 https://doi.org/10.3972/glacier.001.2013.db.

787 Liu, Z., Tian, L., Yao, T., Gong, T., Yin, C., & Yu, W. (2007). Temporal and spatial variations
788 of delta O-18 in precipitation of the Yarlung Zangbo River Basin. Journal of Geographical
789 Sciences, 17(3), 317-326. doi:10.1007/s11442-007-0317-1

790 Lutz, A. F., Immerzeel, W. W., Shrestha, A. B., & Bierkens, M. F. P. (2014). Consistent increase
791 in High Asia's runoff due to increasing glacier melt and precipitation. Nature Climate

792 Change, 4(7), 587-592. doi:10.1038/nclimate2237

793 Masood, M., Yeh, P. J. F., Hanasaki, N., & Takeuchi, K. (2015). Model study of the impacts of
794 future climate change on the hydrology of Ganges–Brahmaputra–Meghna basin.
795 Hydrology and Earth System Sciences, 19(2), 747-770. doi:10.5194/hess-19-747-2015

796 Mcdonnell, J. J. , & Beven, K. . (2014). Debates—the future of hydrological sciences: a
797 (common) path forward? a call to action aimed at understanding velocities, celerities and
798 residence time distributions of the headwater hydrograph. Water Resources Research,
799 50(6).

800 McGuire, K. J., Weiler, M., & McDonnell, J. J. (2007). Integrating tracer experiments with
801 modeling to assess runoff processes and water transit times. Advances in Water Resources,
802 30(4), 824-837.

803 Myneni, R., Knyazikhin, Y., Park, T. (2015). MOD15A2H MODIS/Terra Leaf Area
804 Index/FPAR 8-Day L4 Global 500m SIN Grid V006 [Data set]. NASA EOSDIS Land
805 Processes DAAC. Accessed 2020-01-01 from
806 https://doi.org/10.5067/MODIS/MOD15A2H.006

807 Nan, Y., Tian, L., He, Z., Tian, F., & Shao, L. (2021). The value of water isotope data on
808 improving process understanding in a glacierized catchment on the Tibetan Plateau.
809 Hydrology and Earth System Sciences, 25(6), 3653-3673.

810 Noone, D., & Sturm, C. (2010). Comprehensive Dynamical Models of Global and Regional
811 Water Isotope Distributions.

812 Pu, T., Wang, K., Kong, Y., Shi, X., Kang, S., Huang, Y., . . . Cuntz, M. (2020). Observing and
813 Modeling the Isotopic Evolution of Snow Meltwater on the Southeastern Tibetan Plateau.
814 Water Resources Research, 56(9). doi:10.1029/2019wr026423

815 Rai, S. P., Singh, D., Jacob, N., Rawat, Y. S., & Arora, M. (2019). Identifying contribution of
816 snowmelt and glacier melt to the Bhagirathi River (Upper Ganga) near snout of the
817 Gangotri Glacier using environmental isotopes. Catena, 173, 339-351.

818 Reggiani, P., Hassanizadeh, S. M., Sivapalan, M., & Gray, W. G. (1999). A unifying framework
819 for watershed thermodynamics: constitutive relationships. Advances in Water Resources,
820 23(1), 15-39.

821 Schaner, N., Voisin, N., Nijssen, B., & Lettenmaier, D. P. (2012). The contribution of glacier

822 melt to streamflow. Environmental Research Letters, 7(3). doi:10.1088/1748-
823 9326/7/3/034029

824 Son, K., & Sivapalan, M. (2007). Improving model structure and reducing parameter
825 uncertainty in conceptual water balance models through the use of auxiliary data. Water
826 Resources Research, 43(1). doi:10.1029/2006wr005032

827 Stadnyk, T. A., Delavau, C., Kouwen, N., & Edwards, T. W. D. (2013). Towards hydrological
828 model calibration and validation: simulation of stable water isotopes using the
829 isoWATFLOOD model. Hydrological Processes, 27(25), 3791-3810.
830 doi:10.1002/hyp.9695

831 Sturm, C., Hoffmann, G., & Langmann, B. (2007). Simulation of the stable water isotopes in
832 precipitation over South America: Comparing regional to global circulation models.
833 Journal of Climate, 20(15), 3730-3750. doi:10.1175/jcli4194.1

834 Sturm, K., Hoffmann, G., Langmann, B., & Stichler, W. (2005). Simulation of delta O-18 in
835 precipitation by the regional circulation model REMOiso. Hydrological Processes, 19(17),
836 3425-3444. doi:10.1002/hyp.5979

837 Su, F., Zhang, L., Ou, T., Chen, D., Yao, T., Tong, K., & Qi, Y. (2016). Hydrological response
838 to future climate changes for the major upstream river basins in the Tibetan Plateau. Global
839 and Planetary Change, 136, 82-95. doi:10.1016/j.gloplacha.2015.10.012

840 Tian, F., Hu, H., Lei, Z., & Sivapalan, M. (2006). Extension of the Representative Elementary
841 Watershed approach for cold regions via explicit treatment of energy related processes.
842 Hydrology and Earth System Sciences, 10(5), 619-644. doi:10.5194/hess-10-619-2006

843 Tian, F., Hu, H., & Lei, Z. (2008). Thermodynamic watershed hydrological model: Constitutive
844 relationship. Science in China Series E: Technological Sciences, 51(9), 1353-1369.

845 Tian, F., Xu, R., Nan, Y., Li, K., & He, Z. (2020). Quantification of runoff components in the
846 Yarlung Tsangpo River using a distributed hydrological model.. Advances in Water
847 Science, 31(3), 324-336.

848 Wang, C., Dong, Z., Qin, X., Zhang, J., Du, W., & Wu, J. (2016). Glacier meltwater runoff
849 process analysis using δD and δ 18 O isotope and chemistry at the remote Laohugou
850 glacier basin in western Qilian Mountains, China. Journal of Geographical Sciences, 26(6),
851 722-734.

852 Wang, X., Zhang, X., Zhang, W., Zhang, X., & Luo, Z. (2017). Comparison on Spatial
853 Distribution of Hydrogen and Oxygen Stable Isotope GCM Simulation in Global
854 Precipitation. Advance in Earth Sciences, 32(9), 983-995.

855 Wolfe, B. B., Karst-Riddoch, T. L., Hall, R. I., Edwards, T. W. D., English, M. C., Palmini,
856 R., . . . Vardy, S. R. (2007). Classification of hydrological regimes of northern floodplain
857 basins (Peace -Athabasca Delta, Canada) from analysis of stable isotopes (delta O-18,
858 delta H-2) and water chemistry. Hydrological Processes, 21(2), 151-168.
859 doi:10.1002/hyp.6229

860 Xi, X. (2014). A Review of Water Isotopes in Atmospheric General Circulation Models: Recent
861 Advances and Future Prospects. International Journal of Atmospheric Sciences, 2014, 1-
862 16. doi:10.1155/2014/250920

863 Xu, M., Kang, S., Wang, X., Pepin, N., & Wu, H. (2019). Understanding changes in the water
864 budget driven by climate change in cryospheric - dominated watershed of the northeast
865 Tibetan Plateau, China. Hydrological processes, 33(7), 1040-1058.

866 Xu, R., Hu, H., Tian, F., Li, C., & Khan, M. Y. A. (2019). Projected climate change impacts on
867 future streamflow of the Yarlung Tsangpo-Brahmaputra River. Global and Planetary
868 Change, 175, 144-159. doi:10.1016/j.gloplacha.2019.01.012

869 Xu, R., Tian, F., Yang, L., Hu, H., Lu, H., & Hou, A. (2017). Ground validation of GPM IMERG
870 and TRMM 3B42V7 rainfall products over southern Tibetan Plateau based on a high-
871 density rain gauge network. Journal of Geophysical Research: Atmospheres, 122(2), 910-
872 924. doi:10.1002/2016jd025418

873 Yang, K., He, J., Tang, W., Qin, J., & Cheng, C. C. K. (2010). On downward shortwave and
874 longwave radiations over high altitude regions: Observation and modeling in the Tibetan
875 Plateau. Agricultural and Forest Meteorology, 150(1), 38-46.
876 doi:10.1016/j.agrformet.2009.08.004

877 Yao, T., Masson-Delmotte, V., Gao, J., Yu, W., Yang, X., Risi, C., . . . Hou, S. (2013). A review
878 of climatic controls on δ18O in precipitation over the Tibetan Plateau: Observations and
879 simulations. Reviews of Geophysics, 51(4), 525-548. doi:10.1002/rog.20023

880 Yao, Y., Zheng, C., Andrews, C. B., Scanlon, B. R., Kuang, X., Zeng, Z., ... & Li, G. (2021).
881 Role of Groundwater in Sustaining Northern Himalayan Rivers. Geophysical Research
882 Letters, 48(10), e2020GL092354.

883 Yong, B., Wang, C. Y., Chen, J., Chen, J., Barry, D. A., Wang, T., & Li, L. (2021). Missing water
884 from the Qiangtang Basin on the Tibetan Plateau. Geology.

885 Yoshimura, K., Kanamitsu, M., Noone, D., & Oki, T. (2008). Historical isotope simulation
886 using Reanalysis atmospheric data. Journal of Geophysical Research, 113(D19).
887 doi:10.1029/2008jd010074

888 Zhang, F., Liu, J., Gong, T., & Wang, H. (2006a). Hydrological Regime of the Karuxung
889 Watershed in North Himalayas. Acta Geographica Sinica, 61(11), 1141-1148.

890 Zhang, F., Zhang, H., Hagen, S. C., Ye, M., Wang, D., Gui, D., . . . Liu, J. (2015). Snow cover
891 and runoff modelling in a high mountain catchment with scarce data: effects of
892 temperature and precipitation parameters. Hydrological Processes, 29(1), 52-65.
893 doi:10.1002/hyp.10125

894 Zhang, L., Su, F., Yang, D., Hao, Z., & Tong, K. (2013). Discharge regime and simulation for
895 the upstream of major rivers over Tibetan Plateau. Journal of Geophysical Research:
896 Atmospheres, 118(15), 8500-8518. doi:10.1002/jgrd.50665

897 Zhang, Y., Liu, S., & Ding, Y. (2006b). Spatial variation of degree-day factors on the observed
898 glaciers in western China. ACTA GEOGRAPHICA SINICA-CHINESE EDITION-, 61(1),
899 89.

900 Zhao, L., Xiao, H., Zhou, M., Cheng, G., Wang, L., Yin, L., & Ren, J. (2012). Factors
901 controlling spatial and seasonal distributions of precipitation d18O in China. Hydrological
902 Processes, 26(1), 143-152. doi:10.1002/hyp.8118

903

List of figures

Figure 1. Location and topography of (a) Tibetan Plateau, (b) Yarlung Tsangpo River basin and (c) Karuxung catchment.

Figure 2. The scatter diagrams between original/corrected isoGSM and measured isotope data in YTR basin (subfigures a and b) and KR catchment (subfigures c and d)

Figure 3. Temporal variations of precipitation $\delta^{18}O$ derived from measured and isoGSM data in YTR basin (subfigure a) and KR catchment (subfigure b)

Figure 4. Comparisons of the amount weighted averages of precipitation $\delta^{18}O$ on 63 REWs in the YTR basin by longitude (a) and elevation (b).

Figure 5. Spatial distribution of average precipitation isotope composition obtained by (a) interpolated measurement data and (b) corrected isoGSM.

Figure 6. Uncertainty ranges of discharge (Nuxia station) and SCA simulations in YTR basin during calibration and validation periods produced by the behavioral parameter sets of the dual-objective (subfigure a and b), interpolationt-forced triple-objective (subfigure c and d), and isoGSM-forced triple-objective (subfigure e and f) calibration variants. The discharge data is hidden for the data security policy.

Figure 7. Uncertainty ranges of stream water $\delta^{18}O$ simulations at four stations in 2005 produced by the behavioral parameter sets of the dual-objective (a), interpolation-forced triple-objective (b), and isoGSM-forced triple-objective (c) calibration variants.

Figure 8. Uncertainty ranges of discharge simulations at Yangcun and Nugesha stations produced by the behavioral parameter sets of the dual-objective (subfigure a and b), interpolation-forced triple-objective (subfigure c and d), and isoGSM-forced triple-objective (subfigure e and f) calibration variants.

Figure 9. Uncertainty ranges of discharge and SCA simulations in KR catchment during calibration and validation periods produced by the behavioral parameter sets of the dual-objective (subfigure a and b), interpolation-forced triple-objective (subfigure c and d), and isoGSM-forced triple-objective (subfigure e and f) calibration variants.

Figure 10. Uncertainty ranges of stream water $\delta^{18}O$ simulations in KR catchment during calibration and validation periods produced by the behavioral parameter sets of the dual-objective (a), interpolation-forced triple-objective (b), and isoGSM-forced triple-objective (c) calibration variants.

Figure 11. Average proportion and corresponding uncertainty ranges of different water sources in the annual water input for runoff generation estimated by different calibration variants in (a) YTR and (b) KR catchments.

Figure 12. The relationships between (a) MAE_{iso} and NSE_{dis}, (b) NSE_{dis} and glacier melt contribution and (c) MAE_{iso} and glacier melt contribution.

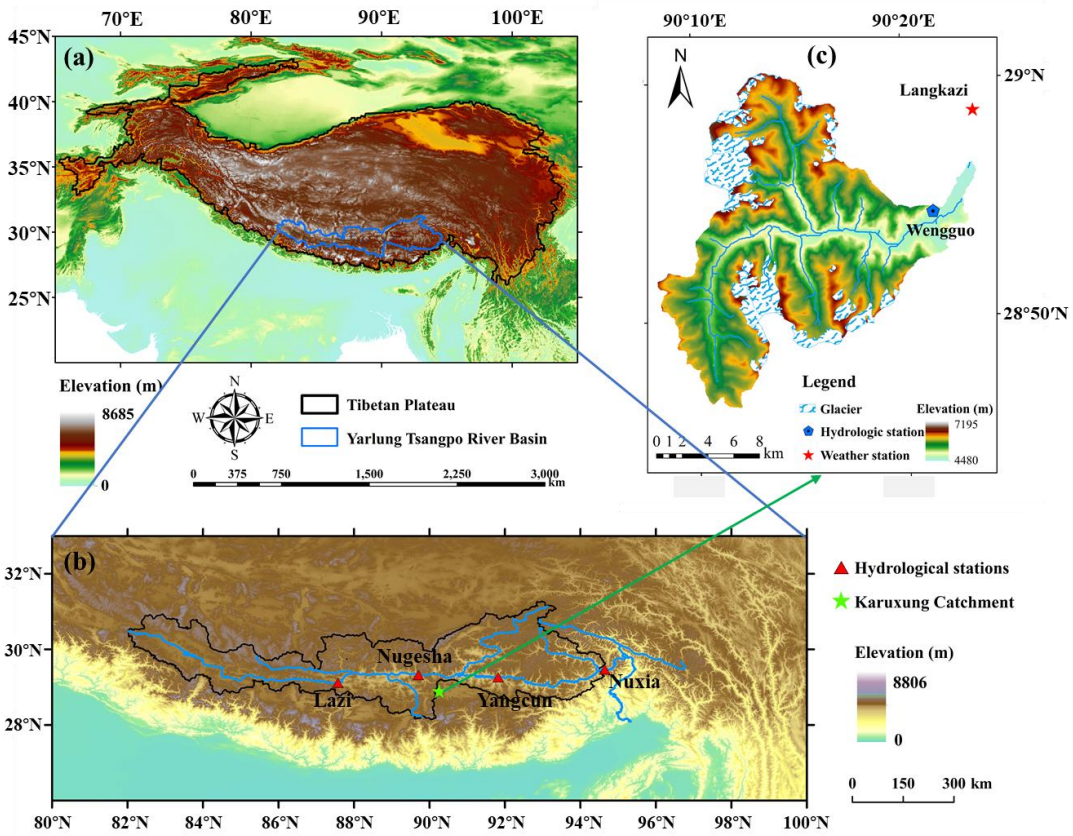

Figure 1. Location and topography of (a) Tibetan Plateau, (b) Yarlung Tsangpo River basin and (c) Karuxung catchment

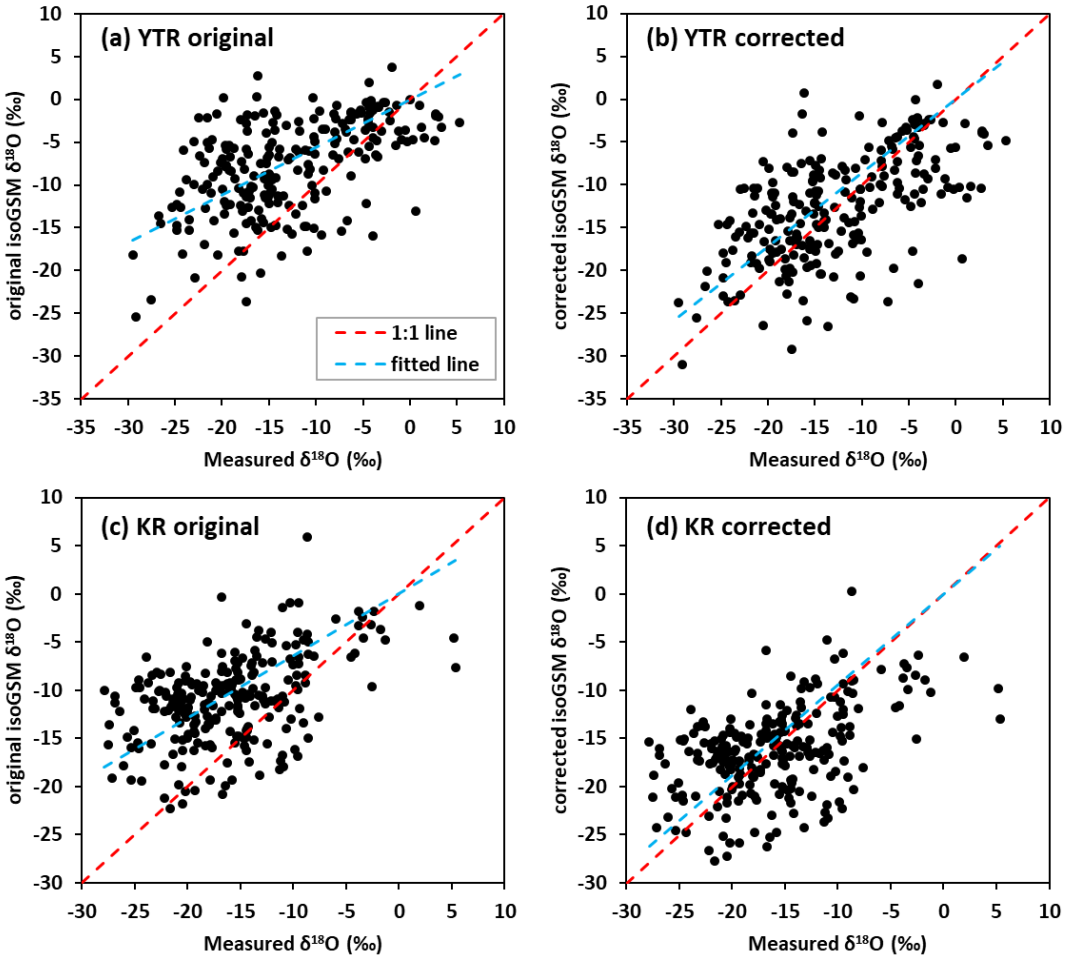

Figure 2. The scatter diagrams between original/corrected isoGSM and measured isotope data in YTR basin (subfigures a and b) and KR catchment (subfigures c and d).

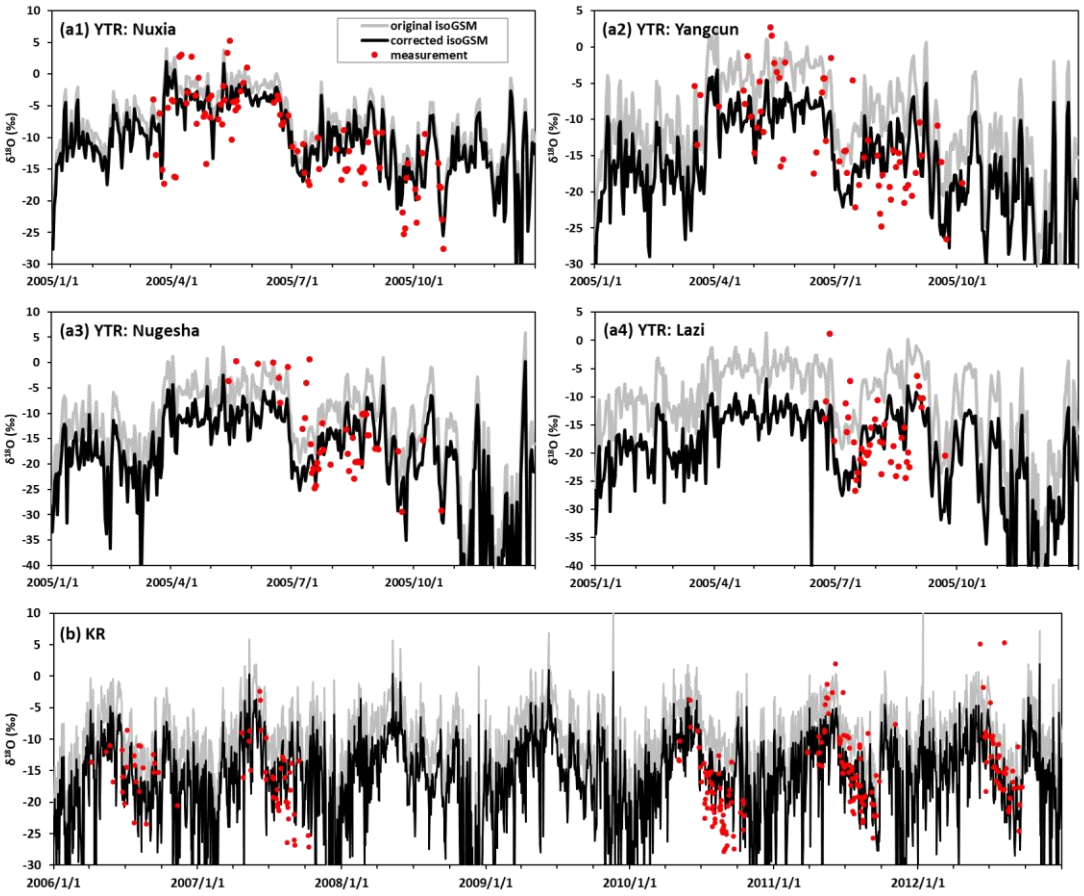

Figure 3. Temporal variations of precipitation $\delta^{18}O$ derived from measured and isoGSM data in YTR basin (subfigure a) and KR catchment (subfigure b).

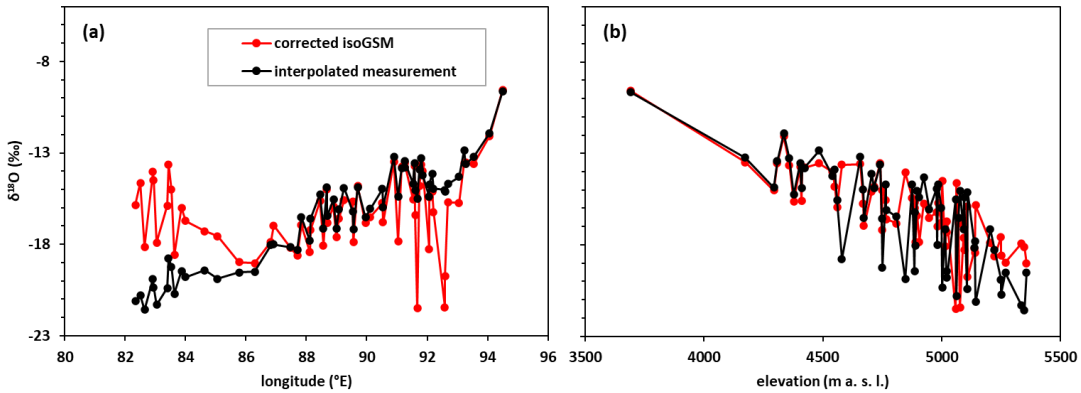

954

955 **Figure 4.** Comparisons of the amount weighted averages of precipitation $\delta^{18}O$ on 63 REWs in
956 the YTR basin by longitude (a) and elevation (b).

957

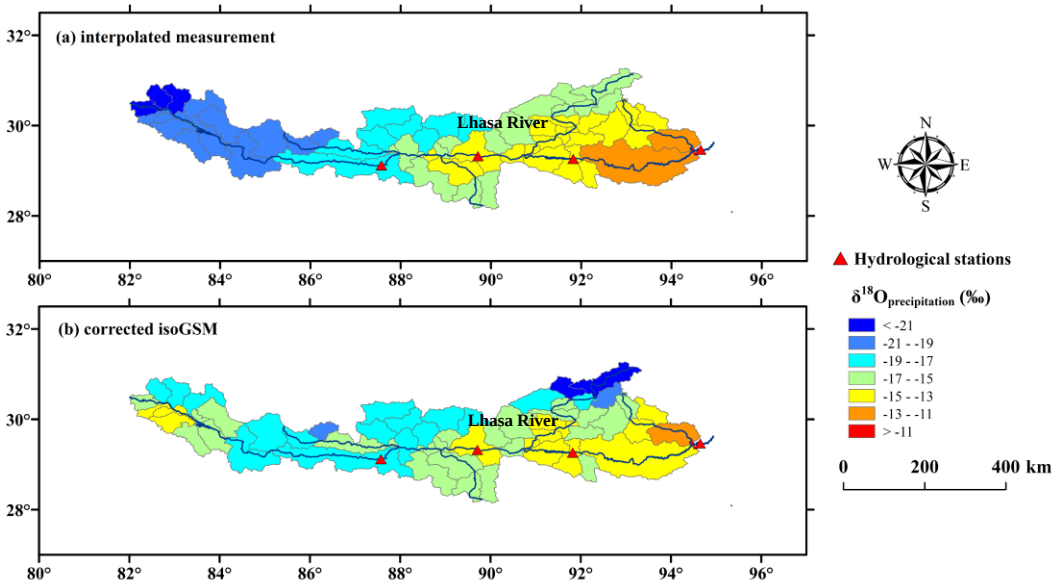

958

959 **Figure 5.** Spatial distribution of average precipitation isotope composition obtained by (a)
960 interpolated measurement data and (b) corrected isoGSM.

961

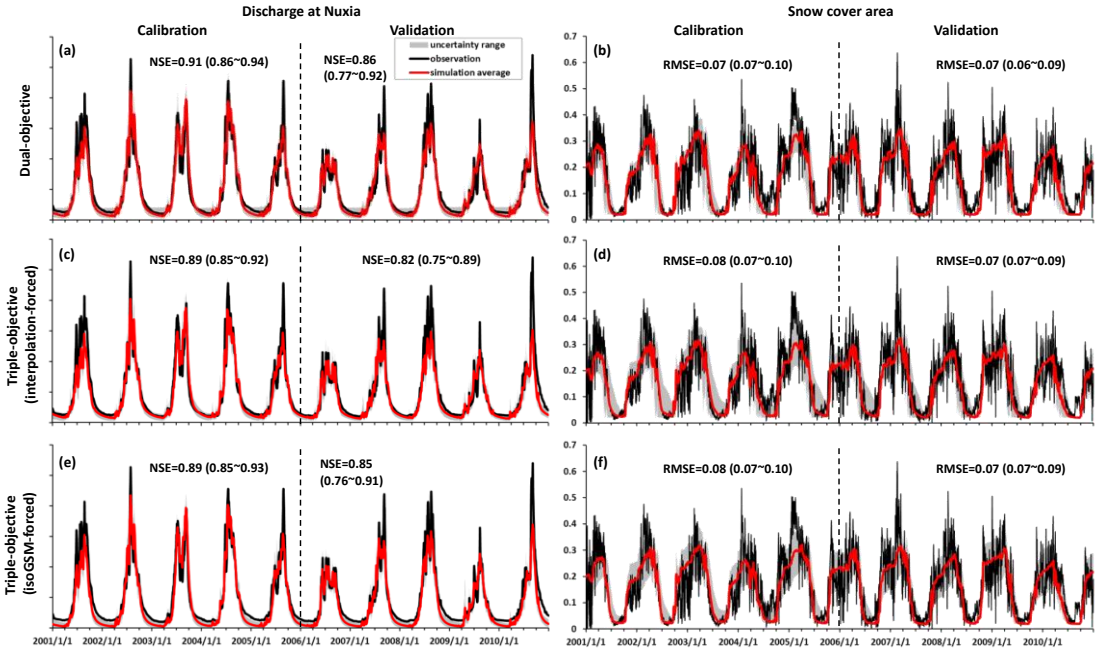

Figure 6. Uncertainty ranges of discharge (Nuxia station) and SCA simulations in YTR basin during calibration and validation periods produced by the behavioral parameter sets of the dual-objective (subfigure a and b), interpolation-forced triple-objective (subfigure c and d), and isoGSM-forced triple-objective (subfigure e and f) calibration variants. The scale of discharge axis is hidden due to data security policy.

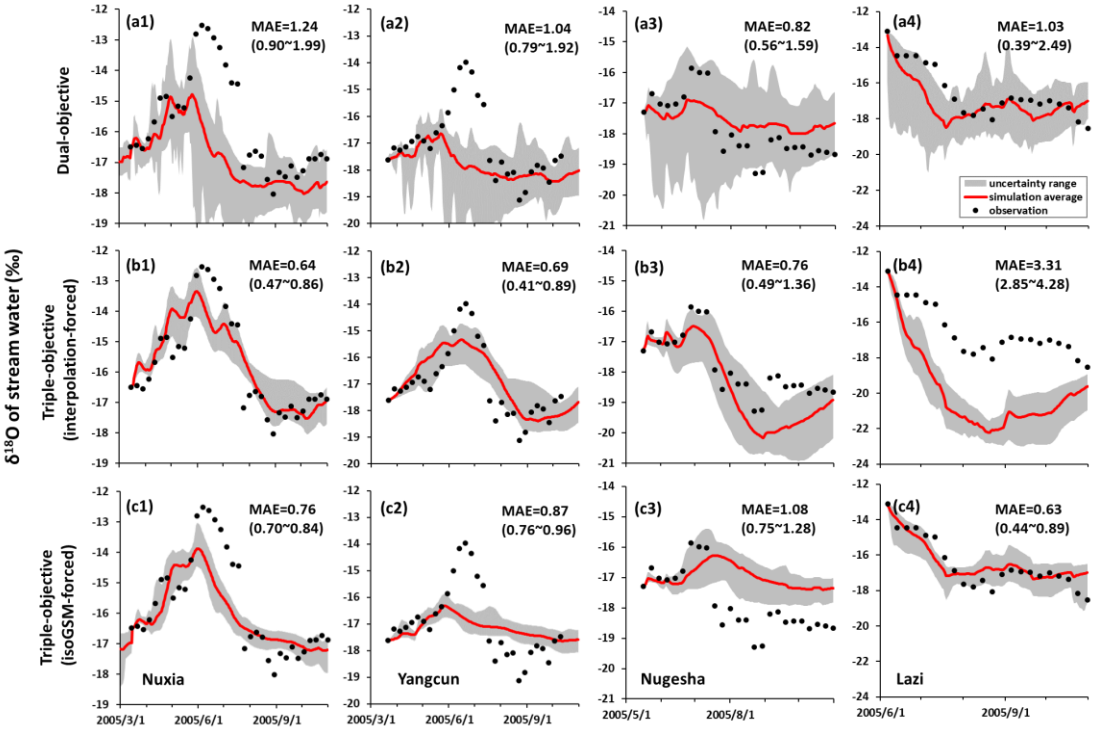

Figure 7. Uncertainty ranges of stream water $\delta^{18}O$ simulations at four stations in 2005 produced by the behavioral parameter sets of the dual-objective (a), interpolation-forced triple-objective (b), and isoGSM-forced triple-objective (c) calibration variants.

977

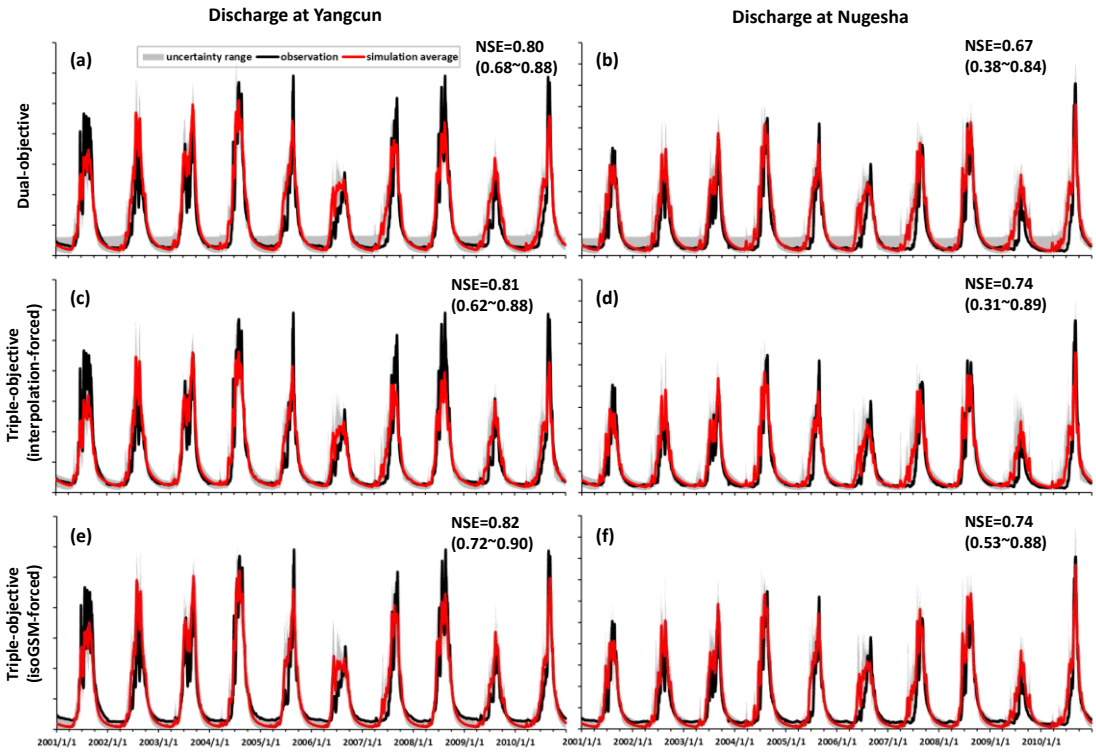

978

979 **Figure 8.** Uncertainty ranges of discharge simulations at Yangcun and Nugesha stations
980 produced by the behavioral parameter sets of the dual-objective (subfigure a and b),
981 interpolation-forced triple-objective (subfigure c and d), and isoGSM-forced triple-objective
982 (subfigure e and f) calibration variants.

983

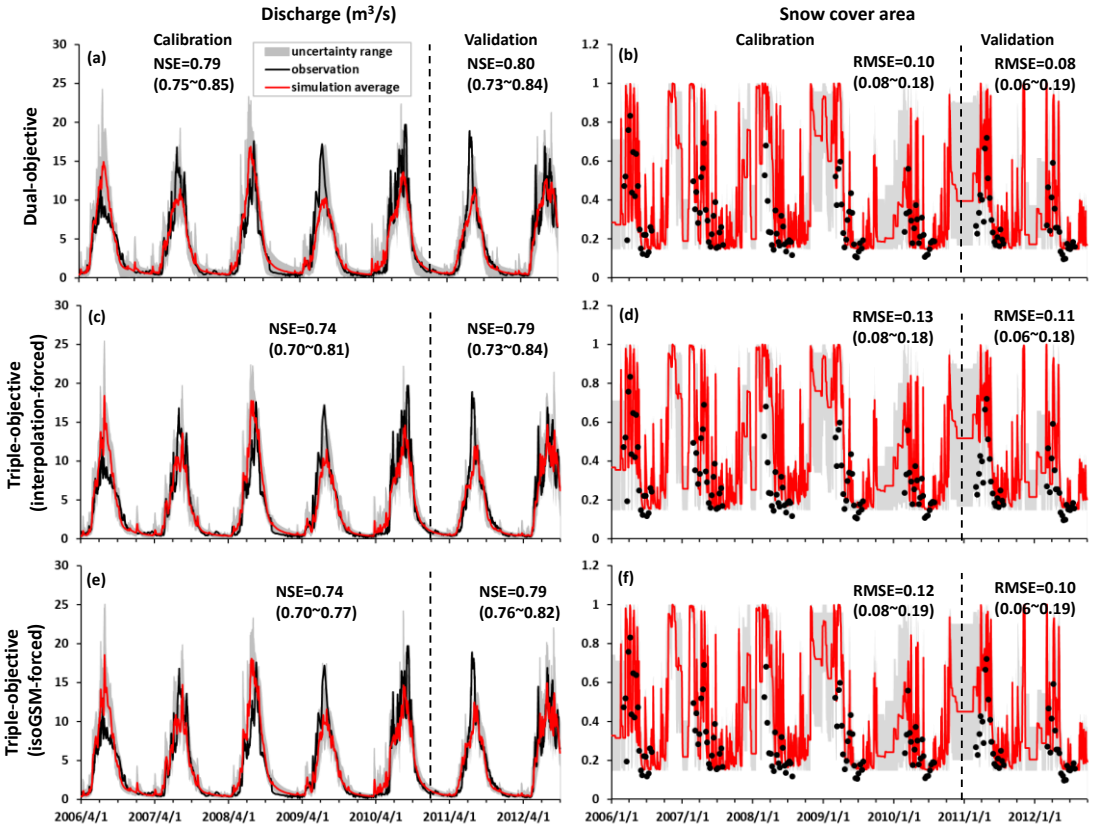

Figure 9. Uncertainty ranges of discharge and SCA simulations in KR catchment during calibration and validation periods produced by the behavioral parameter sets of the dual-objective (subfigure a and b), interpolation-forced triple-objective (subfigure c and d), and isoGSM-forced triple-objective (subfigure e and f) calibration variants.

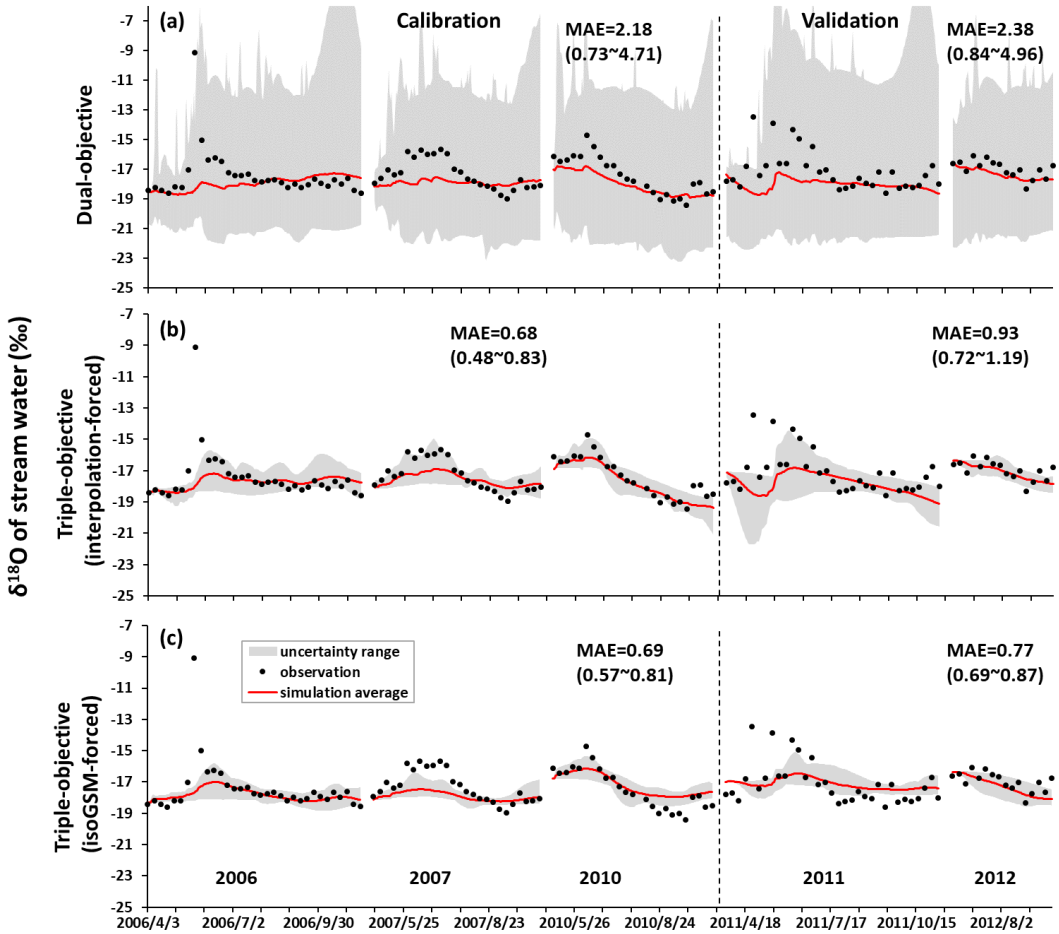

Figure 10. Uncertainty ranges of stream water $\delta^{18}O$ simulations in KR catchment during calibration and validation periods produced by the behavioral parameter sets of the dual-objective (a), interpolation-forced triple-objective (b), and isoGSM-forced triple-objective (c) calibration variants.

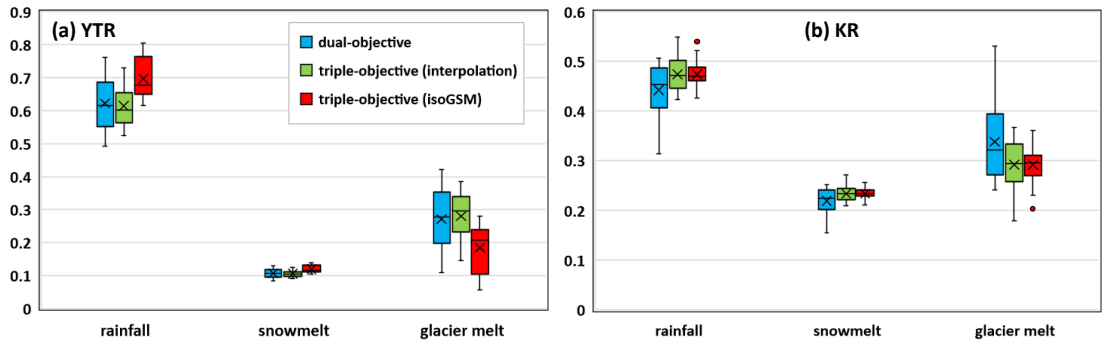

998

999 **Figure 11.** Average proportion and corresponding uncertainty ranges of different water sources
1000 in the annual water input for runoff generation estimated by different calibration variants in (a)
1001 YTR and (b) KR catchments.
1002

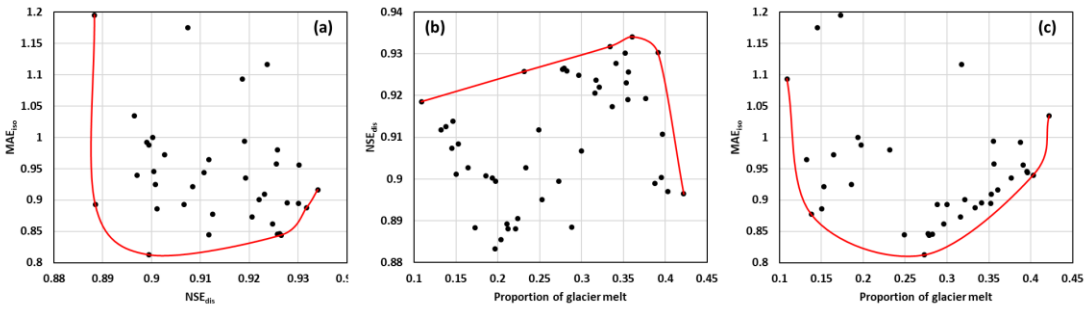

Figure 12. The relationships between (a) MAE_{iso} and NSE_{dis}, (b) NSE_{dis} and glacier melt contribution and (c) MAE_{iso} and glacier melt contribution.

List of tables

Table 1. Characteristics of precipitation and stream water samples in YTR and KR catchments.

Table 2. Calibrated parameters of the THREW-t model.

Table 3. Comparisons of the model performance in YTR basin produced by different calibration variants.

Table 4. Comparisons of the model performance in KR catchment produced by different calibration variants.

Table 5. Average proportions of water sources in the annual and seasonal water inputs for runoff generation in YTR basin.

Table 6. Average proportions of water sources in the annual and seasonal water inputs for runoff generation in KR catchment.

1022 **Table 1.** Characteristics of precipitation and stream water samples in YTR and KR catchments.

Catchment (Station)	Year	Period Dd/mm to dd/mm	Precipitation sample number	Stream sample number
YTR (Nuxia)	2005	14/03 to 23/10	86	34
YTR (Yangcun)		17/03 to 05/10	59	30
YTR (Nugesha)		14/05 to 22/10	45	25
YTR (Lazi)		06/06 to 22/09	42	22
KR (Wengguo)	2006	04/06 to 11/11	24	31
	2007	23/04 to 09/10	39	25
	2010	05/05 to 18/10	63	23
	2011	28/03 to 06/11	69	32
	2012	16/06 to 22/09	42	14

1023

1024 **Table 2.** Calibrated parameters of the THREW-t model

Symbol	Unit	Physical descriptions	Range
nt	-	Manning roughness coefficient for hillslope	0-0.2
WM	cm	Tension water storage capacity, used in Xinanjiang model (Zhao, 1992) to calculate saturation area	0-10
B	-	Shape coefficient used in Xinanjiang model to calculate saturation area	0-1
KKA	-	Coefficient to calculate subsurface runoff in $Rg=KKD \cdot S \cdot K^S_S \cdot (y_S/Z)^{KKA}$, where S is the topographic slope, K^S_S is the saturated hydraulic conductivity, y_s is the depth of saturated groundwater, Z is the total soil depth	0-6
KKD	-	See description for *KKA*	0-0.5
T_0	℃	Temperature threshold above which snow and glacier melt	-5-5
DDF_N	mm/℃/day	Degree day factor for snow	0-10
DDF_G	mm/℃/day	Degree day factor for glacier	0-10
C1	-	Coefficient to calculate the runoff concentration process using Muskingum method: $O_2=C_1 \cdot I_1+C_2 \cdot I_2+C_3 \cdot O_1+C_4 \cdot Q_{lat}$, where I_1 and O_1 is the inflow and outflow at prior step, I_2 and O_2 is the inflow and outflow at current step, Q_{lat} is lateral flow of the river channel, $C_3=1-C_1-C_2$, $C_4=C_1+C_2$	0-1
C2	-	See description for *C1*	0-1

1025

Table 3. Comparisons of the model performance in YTR basin produced by different calibration variants.

calibration variant	**behavioral ratio** [a]	**period /station** [b]	**NSE_{dis}** [c,d]	**$RMSE_{SCA}$**	**MAE_{iso}**
Dual-objective	0.98	calibration	0.91 (0.86-0.93)	0.07 (0.07-0.10)	1.24 (0.90-1.99)
		validation	0.86 (0.77-0.92)	0.07 (0.06-0.09)	0.96 (0.75~1.97)
Triple-objective (measurement)	0.64	calibration	0.89 (0.85-0.92)	0.08 (0.07-0.10)	0.64 (0.47-0.86)
		validation	0.82 (0.75-0.89)	0.07 (0.07-0.09)	1.46 (1.17-1.93)
Triple-objective (isoGSM)	0.82	calibration	0.89 (0.85-0.93)	0.08 (0.07-0.10)	0.76 (0.70-0.84)
		validation	0.85 (0.76-0.91)	0.07 (0.07-0.09)	0.87 (0.76-1.04)

a: Behavioral ratio represents the ratio of behavioral parameter set number to the run time of pySOT program.

b: "Period" for discharge and SCA simulation, and "station" for isotope simulation.

c: Bracketed values represent the minimal and maximal values produced by the behavioral parameter sets.

d: NSE_{dis} is calculated based on the simulated and observed streamflow at Nuxia station

1035 **Table 4.** Comparisons of the model performance in KR catchment produced by different
1036 calibration variants.

calibration variant	behavioral ratio	period	NSE_{dis}	$RMSE_{SCA}$	MAE_{iso}
Dual-objective	0.78	calibration	0.79	0.10	2.18
			(0.75-0.85)	(0.08-0.18)	(0.73-4.71)
		validation	0.80	0.08	2.38
			(0.73-0.84)	(0.06-0.19)	(0.84-4.96)
Triple-objective (measurement)	0.13	calibration	0.74	0.13	0.68
			(0.70-0.81)	(0.08-0.18)	(0.48-0.83)
		validation	0.79	0.11	0.93
			(0.73-0.84)	(0.06-0.18)	(0.72-1.19)
Triple-objective (isoGSM)	0.12	calibration	0.74	0.12	0.69
			(0.70-0.77)	(0.08-0.19)	(0.57-0.81)
		validation	0.79	0.10	0.77
			(0.76-0.82)	(0.06-0.19)	(0.69-0.87)

1037

Table 5. Average proportions of water sources in the annual and seasonal water inputs for runoff generation in YTR basin.

Season	Water source [a]	Dual-objective	Triple-objective (measurement)	Triple-objective (isoGSM)
Annual	Rainfall	62.2	61.4	69.6
	Snow melt	10.7	10.6	12.0
	Glacier melt	27.1	28.0	18.4
	Uncertainty	11.4	8.6	8.9
Spring	Rainfall	35.4	36.8	44.2
	Snow melt	42.9	39.7	43.8
	Glacier melt	21.7	23.5	12.0
	Uncertainty	13.4	12.8	11.8
Summer	Rainfall	69.8	68.2	74.5
	Snow melt	3.4	4.4	6.4
	Glacier melt	26.8	27.4	19.1
	Uncertainty	10.2	7.9	8.7
Autumn	Rainfall	63.1	61.9	76.1
	Snow melt	3.5	3.5	2.7
	Glacier melt	33.5	34.7	22.0
	Uncertainty	16.1	12.8	13.3
Winter	Rainfall	11.9	12.8	30.8
	Snow melt	70.1	65.8	61.7
	Glacier melt	18.0	21.4	7.5
	Uncertainty	19.7	20.6	30.8

a: The uncertainty of the contribution is defined as $E = \sqrt{{E_R}^2 + {E_N}^2 + {E_G}^2}$, where E_R, E_N and E_G represent the standard deviations of the contributions of the water sources produced by the corresponding behavioral parameter sets. Subscripts of R, N and G represent rainfall, snow meltwater and glacier meltwater, respectively.

1045 **Table 6.** Average proportions of water sources in the annual and seasonal water inputs for
1046 runoff generation in KR catchment.

Season	Water source	Dual-objective	Triple-objective (measurement)	Triple-objective (isoGSM)
Annual	Rainfall	44.2	47.4	47.4
	Snow melt	22.0	23.4	23.4
	Glacier melt	33.8	29.2	29.2
	Uncertainty	9.4	6.2	4.7
Spring	Rainfall	4.1	4.5	4.5
	Snow melt	56.3	61.6	60.9
	Glacier melt	39.5	33.9	34.6
	Uncertainty	13.7	14.2	12.0
Summer	Rainfall	53.5	56.6	56.9
	Snow melt	14.0	15.2	15.1
	Glacier melt	32.4	28.2	28.0
	Uncertainty	9.7	5.1	3.9
Autumn	Rainfall	30.9	35.0	34.3
	Snow melt	33.9	35.3	35.5
	Glacier melt	35.1	29.7	30.3
	Uncertainty	11.2	11.0	9.6
Winter	Rainfall	0	0	0
	Snow melt	55.3	63.3	58.9
	Glacier melt	44.7	36.7	41.1
	Uncertainty	22.3	31.5	29.2

1047